Progress in Additive Manufacturing (2026) 11:3337–3357
https://doi.org/10.1007/s40964-025-01522-6

RESEARCH

Influence of in-situ thermal conditions on the microstructure and mechanical anisotropy of WAAM-fabricated 316LSi structures

Sharath P. Subadra[1] · Kane F. ter Veer[2] · Eduard Mayer[1] · Suresh Alaparthi[1] · Roy Skaria[1] · Christian Klötzer-Freese[3] · Moritz Braun[2] · Shahram Sheikhi[1]

Received: 4 November 2025 / Accepted: 30 December 2025 / Published online: 27 January 2026

Abstract

Wire arc additive manufacturing (WAAM), a subset of additive manufacturing, is emerging as a viable method for fabricating metallic parts. Among the filler materials used, austenitic stainless steel 316LSi is notable for its corrosion resistance and mechanical properties, making it suitable for industries such as transport and oil and gas. However, WAAM-fabricated 316LSi components often exhibit anisotropic behavior at both micro and macro levels. This study investigates the influence of in-situ thermal conditions—specifically melt pool temperature and cooling rates—on the microstructure and mechanical properties of WAAM-produced structures. Walled structures were fabricated using the cold metal transfer (CMT) variant of WAAM. Melt pool behavior was monitored using a high dynamic range (HDR) camera, while thermocouples were employed to determine temperature gradients. Post-deposition surface features were analyzed using parameters such as R-profile and P-profile, along with waviness matrices, to reconstruct surface morphology under varying welding parameters. Microstructural analysis revealed the presence of lathy and skeletal ferrites in an austenitic matrix, with approximately 7% δ-ferrite formed due to rapid interlayer cooling. Mechanical testing indicated directional dependence: samples cut parallel to the deposition direction exhibited higher yield strength (Rp0.2) and tensile strength (Rm) than those cut perpendicularly, although toughness was lower compared to wrought samples. Hardness profiling across the wall thickness showed an increase from bottom to top, correlating with thermal gradients. These findings highlight the impact of thermal conditions on anisotropy in WAAM components and underscore the need for further investigation into optimizing processing parameters to improve structural performance.

Keywords Wire arc additive manufacturing · Machine learning · Weld pool monitoring · Temperature gradients · Mechanical characterisations

✉ Sharath P. Subadra
sharath.peethambaransubadra@haw-hamburg.de

✉ Shahram Sheikhi
shahram.sheikhi@haw-hamburg.de

Kane F. ter Veer
kane.terveer@dlr.de

Eduard Mayer
Eduard.Mayer@haw-hamburg.de

Suresh Alaparthi
Suresh.Alaparthi@haw-hamburg.de

Roy Skaria
Roy.Skaria@haw-hamburg.de

Christian Klötzer-Freese
C.Kloetzer@mmg-propeller.de

Moritz Braun
moritz.braun@dlr.de

1 University of Applied Science Hamburg, Hamburg, Germany

2 Institute of Maritime Energy Systems, German Aerospace Center, Geesthacht, Germany

3 Mecklenburger Metallguss GmbH, Waren (Müritz), Germany

1 Introduction

As an alternative to traditional production techniques, additive manufacturing (AM) has been expanding quickly to produce a variety of intricate designs. AM is an effective technique because it can be used to produce any type of near-net form structures with predetermined proportions. It involves printing a structure layer by layer based on a design in CAD (computer-aided design) software. As an alternative to traditional production techniques, AM has been expanding quickly to produce a variety of intricate designs. A subclassification of AM called direct metal deposition (DMD) makes it possible to produce metallic material structures. DMD can fuse the feedstock material into a final shape by using heat sources such as electric arcs, lasers, or electron beams. When compared to alternative laser or electron beam DMD processes, wire arc additive manufacturing (WAAM) exhibits advantages. It is cost-effective, has high deposition rates, and can be used to construct and/or repair large-scale metallic components with intricate geometries [1–7].

Austenitic stainless steel, particularly grade 316LSi, is widely used in the chemical, nuclear, and maritime industries due to its excellent corrosion resistance, mechanical performance, and weldability. Consequently, it has also become a common feedstock material in the WAAM process. WAAM is a complex welding-based additive manufacturing technique whose quality is strongly influenced by heat flow, microstructure evolution, and the intrinsic properties of the wire. These interdependencies highlight the need for further research to support industrial adoption. This is especially relevant when 316LSi is used as the deposition material, as studies have reported macro- and microscale anisotropy in the resulting components. Such behavior requires deeper investigation, particularly to establish clear correlation with temperature gradients. Additionally, the rapid cooling experienced between successive layers and the associated phase transformations must be examined in greater detail [7]. With improved understanding and control, structural applications of DMD-produced components that meet established standards and safety requirements become achievable [8–10].

Since the majority of welding irregularities are linked to heat input and thermal history, online weld pool monitoring during the WAAM process is of common interest [11]. The geometric dimensions of the part being created are influenced by the weld pool and are inherited from it. This is due to the interplay of material characteristics, inter-pass temperature, deposition rate, travel speed, and arc power [12]. There are many ways to observe the weld pool, including pyrometers [14], optical sensors, and infrared sensors [13]. Using a high dynamic range (HDR) camera, which employs state-of-the-art photographic technology to capture a greater range of brightness levels in a single shot, is an additional method of viewing the weld pool. This improves clarity and details in the darkest shadows as well as the brightest highlights. A better knowledge of melt pool dynamics is made possible by HDRs' easy deployment in production contexts and their capacity to generate clear images that can differentiate between melt pool shape and arc [15]. Because of these benefits, the current study will use a HDR camera, to monitor the weld pool and observe the thermal gradients within each layer.

Studying the heat input and cooling rates during the deposition of each layer in a WAAM process is crucial, in addition to comprehending the melt pool properties. This is due to the process's significant thermal balance, which might compromise the structural integrity of the created structure if a good heat management approach isn't used [16]. A positive energy balance, which suggests higher heat input rather than enough heat sinking, is the cause of the heat accumulation. The component temperature rises with each pass; this characteristic occurs in other AM systems as well as WAAM. A growing quantity of heat is released into the environment during the deposition process through radiation and convection, but direct conduction to a cool substrate is more efficient. As a result, more heat is accumulated because the cooling process is slowed down, due to lower thermal conductivity of the warm sub-layers [17]. Knowing the structure's cooling rates in advance allows for the development of efficient cooling strategies therefore this article attempts to record the temperature field of the wall being printed.

When using WAAM-based manufacturing processes, the structure's surface characteristics (waviness and roughness) and methods for managing it are crucial [18]. Because of the high layer heights, the roughness is more noticeable because these can be viewed as stair steps that appear between two successive layers [19]. The surface quality of WAAM-based products is lower than that of powder-based additive manufacturing techniques; thus, a comprehensive surface characterization is necessary to satisfy structural and industrial criteria [20]. It is necessary to create an appropriate technique for characterizing the surface, and the information gathered from this process will also aid in optimizing the weld parameters. The obtained data can be used to train machine learning models that forecast the ideal parameters for improved surface characteristics [21]. To evaluate the efficacy of the parameters employed in this research, the current study intends to use a profilometer to collect data regarding bead radius and inter-layer height. Eventually, the captured data will be utilized to train machine learning models that will be employed in the ongoing project.

Additive manufacturing through WAAM inherently produces structures/components with distinct thermal histories

Table 1 Chemical composition of wire (wt. %)[28]

	Cr	Ni	Mo	Mn	Si	C	N	Nb	P	Fe
316LSi	18.65	11.64	2.29	1.76	0.65	0.026	0.035	0.016	0.003	64.62

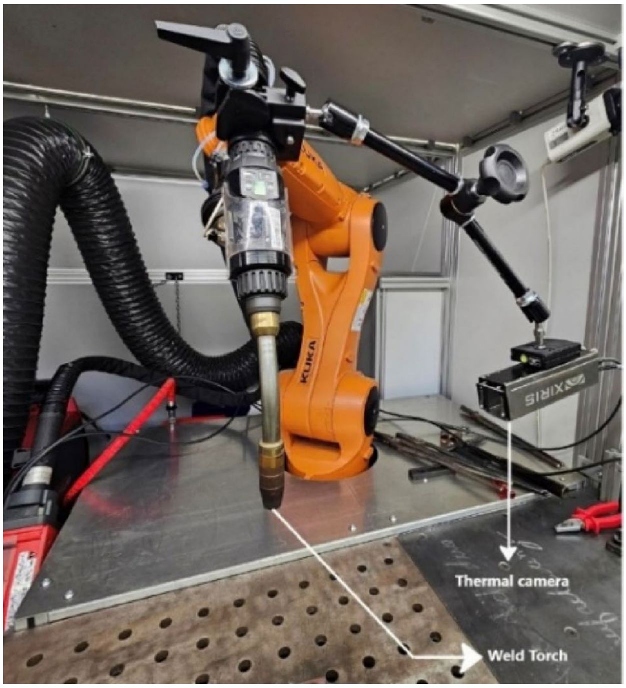

Fig. 1 Equipment setup

which gives rise to microstructural anisotropy, particularly in 316LSi stainless steel. Prior studies have shown that strong directional heat flow and repeated thermal cycle promote epitaxial grain growth, resulting in elongated columnar grains aligned with the build direction [22, 23]. This anisotropic grain morphology directly affects mechanical performance, which aligns with observations that the directional mechanical properties of samples extracted from WAAM components consistently exhibit intrinsic anisotropy [24–27]. Due to this anisotropy, reported mechanical test results vary considerably: some studies indicate greater yield strength along the scan direction, others along the build direction, while several report similar ultimate tensile strengths but reduced elongation and yield strength in the build direction [24–26]. These variations have been attributed to the non-equilibrium microstructure characteristic of WAAM, although a definitive structure–property correlation remains elusive [27]. WAAM 316LSi typically exhibits a mixture of δ-ferrite within an austenitic matrix, accompanied by a combination of columnar and equiaxed grain-features known to influence anisotropic mechanical response [7]. Collectively, these factors underscore the need for a deeper investigation into the process-structure–property relationships governing WAAM 316LSi, as existing literature has yet to establish a comprehensive correlation between thermal history, including local temperature and temperature gradients, microstructure evolution, and the resulting mechanical behavior.

This study is a follow-up to a previous paper that used machine learning (ML) models to determine the best WAAM parameters [28]. By using the random forest approach and linear regression, a combination of parameter sets were found. Weld input parameters, including voltage, current, wire feed rate, and robot travel speed, were obtained through experiments, and the output was the weld bead shape. Four parameters were ultimately determined to be ideal for fabricating structures after the data was utilized to train a machine learning algorithm. The purpose of this study is multifaceted, firstly to investigate the weld pool temperatures of the previously determined parameters. Subsequently, the cooling rates were observed while the walls are being fabricated, and the resulting surface characteristics examined once the fabrication was over. Additionally, by examining the amount of ferrite present and its relationship to temperature gradients, a correlation between the microstructure and mechanical properties (hardness and tension testing) will be assessed. Thus, the optimality of the parameters will be established to further increase the feasibility of employing ML models to expedite the WAAM process and generate near net form structures.

2 Materials and methods

2.1 Materials and fabrication of multi-layered structures

316LSi stainless steel wire of diameter 1.0 mm was used as the feedstock material, which was deposited on commercial steel plates (S355) of dimensions 250 × 80 × 10 mm respectively. Table 1 displays the wire's chemical composition as determined by energy dispersive X-ray spectroscopy (EDX) [28]. A 6-axis robot arm (KUKA KR 6 R900) was used as a handling system to move the welding torch which deposits the feedstock layer-by-layer (see Fig. 1). As depicted in Fig. 1, a HDR camera was attached to the robot arm to observe weld pool in welding direction. Three wall plates of dimensions 140 × 6 × 160 mm were fabricated simultaneously (see Fig. 2C). Each layer was air cooled to an interpass temperature of 50 °C, thus being the start temperature for each layer. A gas metal arc welding process using a power source, Fronius TPS400i was employed along with

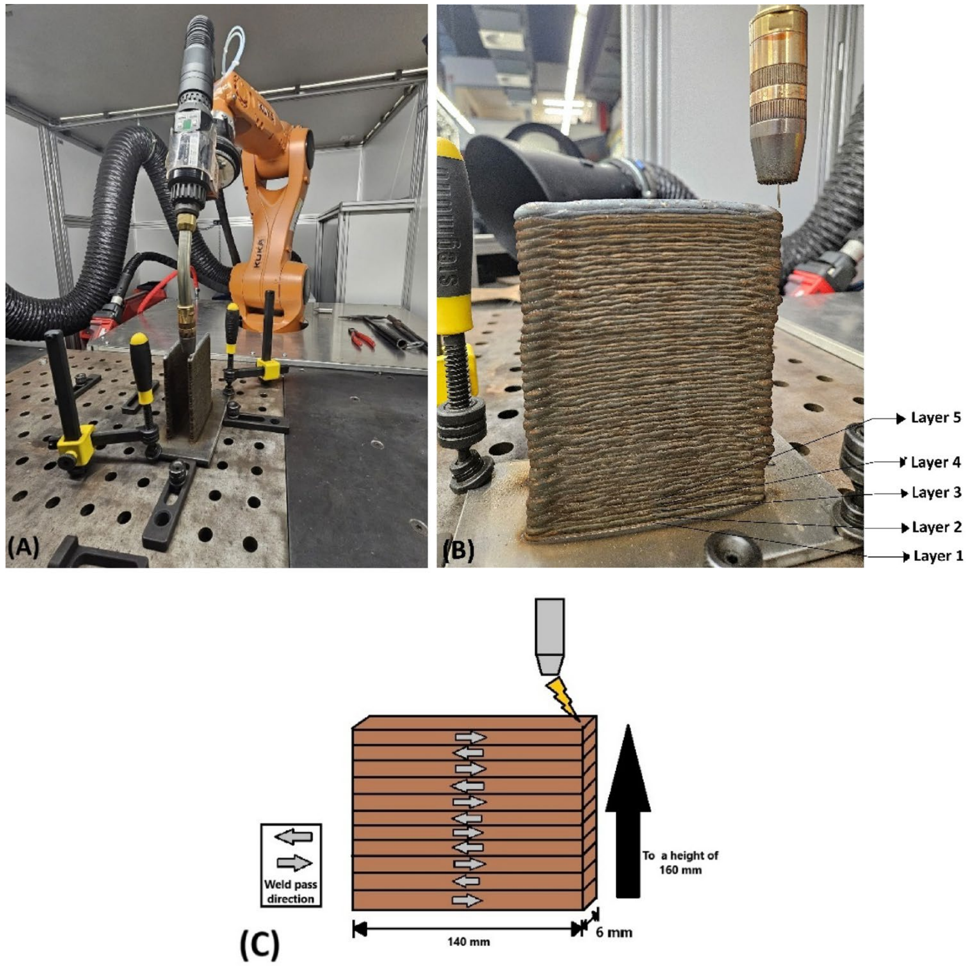

Fig. 2 WAAM set-up **A** Overview of printed structures, **B** Side view of printed wall, **C** Weld strategy

Table 2 Parameters used for fabrication of a multi-layered structure

Layer no	Current [A]	Voltage [V]	Wire feed rate [mm/min]	Robot travel speed [mm/min]	Heat input [kJ/mm]
1st	149	15.6	9	300	7.74
2nd	148	15.2	9	360	6.24
3rd	124	13.9	7.5	360	4.78
4th…n	117	13.3	7	360	4.32

the shield gas consisting of 2% CO_2 and 98% argon, where a flow rate of 12 L/min was adopted.

A parametric study conducted in a previous work [28] identified four optimal parameter sets (summarised in Table 3 of [28]), which are reproduced in Table 2 of this study. Their implementation is illustrated in Fig. 2B, while Fig. 2A presents the fabricated wall with all fixtures in place. The welding strategy shown in Fig. 2C was followed. For the first layer, the parameters specified for Layer 1 in Table 2 were used. The parameters were then progressively adjusted up to Layer 4, as outlined in the table. From Layer 5 onward, the same parameters applied to Layer 4 were maintained. Each deposited layer was air-cooled to a start temperature of 50 °C before the next pass.

2.2 Temperature measurements and weld pool monitoring system

The interpass temperature was measured using k-type thermocouple, which were welded in a manner as seen in Fig. 3A. These thermocouples have an accuracy of approximately ± 2.2 °C. A total of 8 thermo-elements were used, the placements of the same was in such a way that, the temperature on the base, along with the layer temperature will be known. Whereas to observe the weld pool, a Xiris HDR weld camera XVC-1100, a digital camera for weld arc monitoring was used (see Fig. 3B). The camera comes with a custom-made software to monitor the weld pool with different programs inbuilt. One of them involves a line program where the temperature along the line corresponding to the entire length of the weld path will be monitored.

2.3 Surface and mechanical characterisations

The surface characterisation was performed using a 3D profilometer from Keyence (KEYENCE Deutschland GmbH). The profilometer from the VR-6000 series is a fast, high

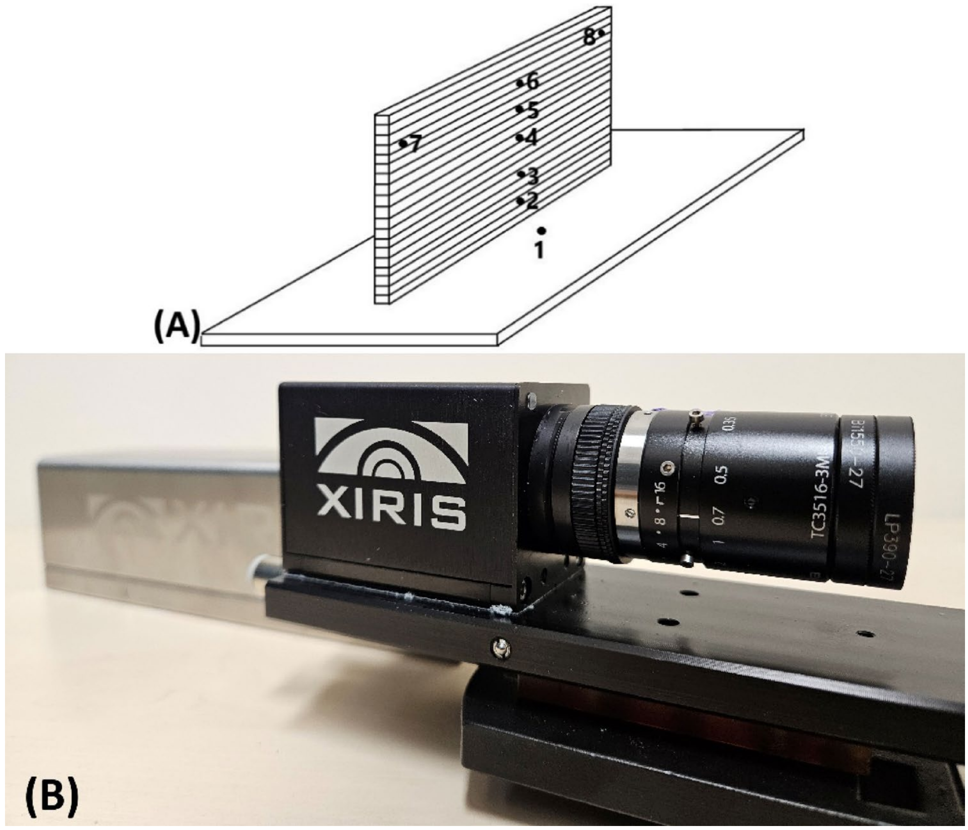

Fig. 3 Temperature measurement. **A** The structure with thermos-elements **B** An Xiris camera system

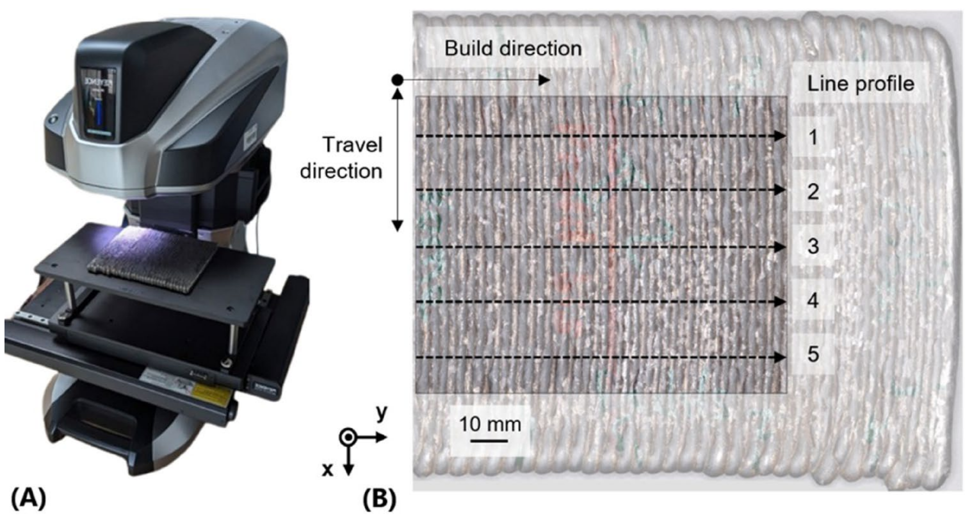

Fig. 4 **A** VR-6000 Profilometer used in the surface scans and **B** 316LSi WAAM sample showing the scanned area and line profiles

precision 3D profile measuring system that has the capability to record glossy surfaces due to its HDR recording algorithm. The measurement accuracy according to the manufacturers specifications is ± 4 µm in the vertical (z) and ± 5 µm in the horizontal (x and y) dimensions. Figure 4A shows the VR series used for the current study along with the scan strategy (Fig. 4B). Surface scans were carried out at 12 × magnification using stitching to join adjacently measured sections. This comprised an 80 × 100 mm area, chosen to avoid edge surface effects and excessive bulging in the upper most section of the wall. 44 complete layers are evaluated in each line profile. The reference plane at z = 0 is defined as the two-dimensional plane fitted to the scanned surface topology using least squared method. Five separate line profiles were evaluated at 15 mm spacings along the travel direction and spanned the 100 mm length of the area in the build direction.

Once the structural part was fabricated, mechanical (tensile) tests at room temperature were performed according to ISO 6892 [29] standard. The tests were performed on a

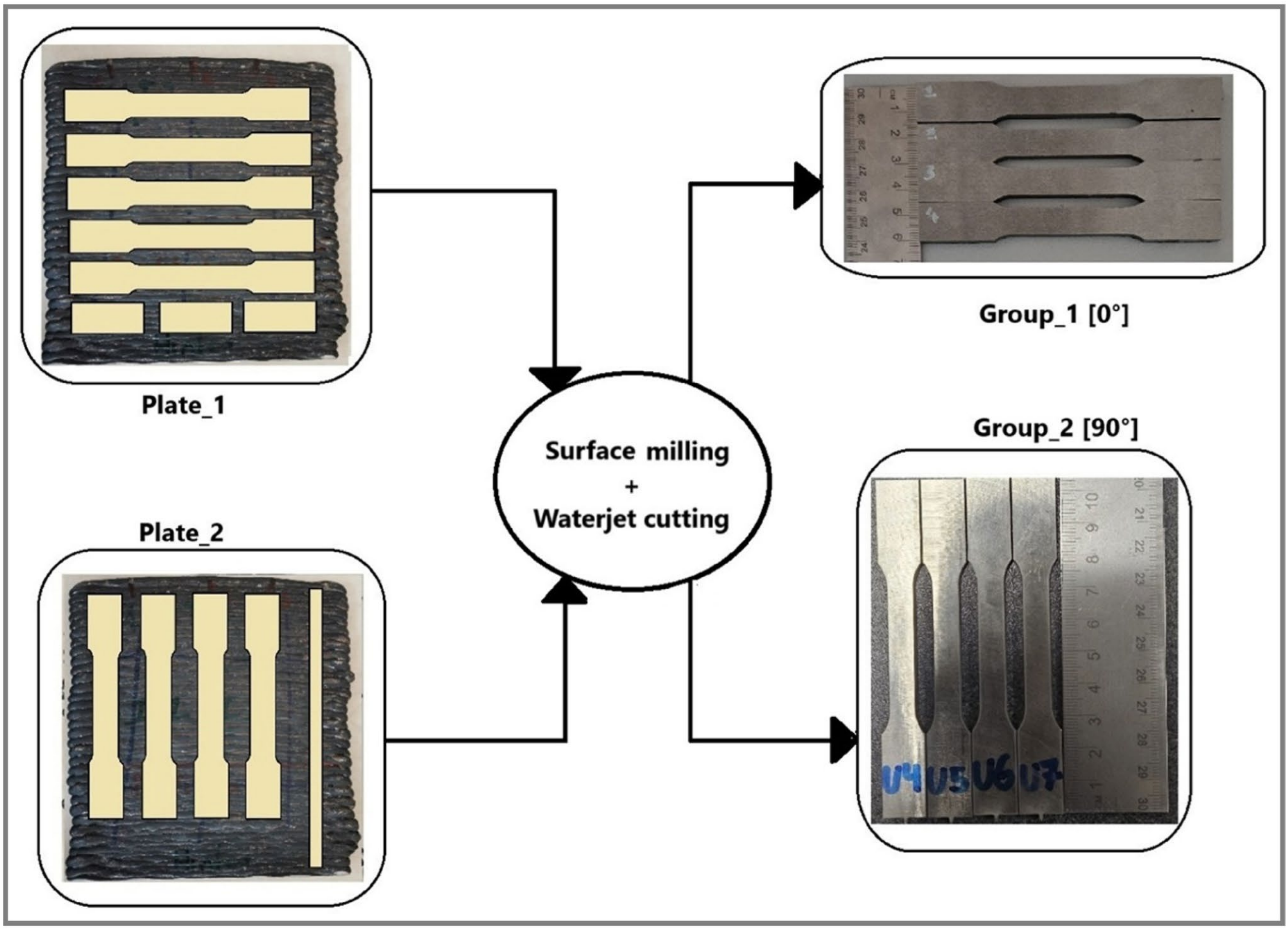

Fig. 5 Illustration of sample geometry from WAAM plates

Table 3 Specimen dimensions in mm

Thickness a_o	Width of parallel length b_o	Gauge length L_o	Parallel length L_c	Total length L_t
4	10	35	45	120

Quasar 200 tensile testing machine with a maximum load cell capacity of 200 kN, and the machine is equipped with a motor drive mechanism. A hydraulic-powered wedge-gripping mechanism is implemented in the machine to avoid slippages, and here the hydraulic holding force can be increased based on user requirements. The plates seen in Fig. 5, were initially milled to a thickness of 4 mm and subsequently samples were cut using water jet equipment, the final dimensions of the samples are as seen in Table 3. The hardness measurements were performed on a Vickers hardness tester (ZwickRoell GmbH & Co. KG) in accordance with the DIN EN ISO 6507-1 [30] standard. A diamond shaped test pyramid is used as an indenter, pressed onto the surface of the material with a set test force for a certain time (10-15 s). The test force was set to HV30, this is due to the strength of the material used. The hardness tests were carried out on plate_2 on a long strip cut from the right edge of the plate. The indentation for the hardness was performed in the thickness region from the base of the strip in a regular interval of 5 mm, this was to ascertain the effect of thermal gradients within the structure.

3 Surface characterisation methods

The surface characteristics of WAAM manufactured thin-walled structures exhibit a clearly visible layered appearance due to the layer-by-layer material deposition. This effect is more apparent in WAAM than in other common AM processes such as LPBF or laser-based DED methods due to the larger melt pool size, energy input and deposition rate [31]. This leads to the formation of notches at the layer boundaries, acting as stress raisers reducing the fracture and fatigue strength of the component [32]. Furthermore, deviations in form are common due to the random occurrence of bulging and material overlapping, where components may require significant material removals in the form milling, grinding and subtractive manufacturing processes [33]. Surface characterization for technical parts is commonly done using geometrical product specifications (GPS), defined in European standards ISO 4287 and ISO 4288 [34, 35]. Here, the as-measured surface profile (P-profile) is filtered to separate the profile into waviness (W-Profile) and roughness (R-profile), see Fig. 6.

The R-profile—separated from the P-profile through applying a high-pass gaussian filter—is composed of small wavelength surface features and mainly used to describe post-mechanical surface treatment or machining. The W-profile on the other hand is the mid wavelength profile features, typically used to characterize surface features such as those from periodic vibrations during manufacturing [36]. Band-pass filtering is used to isolate profile features using upper and lower cut-off wavelengths, defined through λ_c and λ_f for W-profiles in ISO 4287 [34]. This enables the isolation of waviness features from the R-profile and error from the form profile. Additionally, measurement noise is able to be filtered from the R-profile through λ_s. Defining the cut-off wavelengths is a critical step to ensure the profiles are filtered suitably according to the different profiles; however, this is often subjective and dependent on the combination of surface features within the profile as well as on the purpose of the investigation. Recent studies focusing on the characterization of WAAM surface waviness found that the standards were of limited use in defining the cut-off wavelengths due to the random and deterministic nature of the surface geometry, which is influenced mostly by the deposition strategy, welding parameters and feed-material [31, 32]. Two metrics defined in [34] are commonly used to describe the waviness of technical surfaces and will be considered in this study. Firstly, the arithmetical mean height of the W-profile is expressed as:

$$\mathrm{W}_a = \frac{1}{l_r}\int_0^{l_r} |\mathrm{z}(x)|\,dx \tag{1}$$

where, l_r is defined as the sampling length along the line profile, which for R- and W-profiles is equal to their respective upper cut-off wavelengths. $\mathrm{z}(x)$ is the profile height along the line profile within the respective sampling length. Secondly, the maximum height $\mathrm{W_z}$ of the profile is defined as sum of the respective maximum $\mathrm{W_p}$ and minimum $\mathrm{W_v}$ absolute profile heights within the respective sampling length:

$$\mathrm{W_z} = \mathrm{W_p} + \mathrm{W_v} \tag{2}$$

Following the ISO standards, W_a and W_z are generally calculated by averaging along 5 sampling lengths within the total evaluation length l_n. This aims to reduce the influence of outliers or surface anomalies. However, there are no well-defined rules for determining this for the W-profile.

4 Results and discussions

4.1 Cooling rates and weld pool monitoring

The temperature evolution over time is schematically represented in Fig. 7 at various points on the wall, which are designated as measurement sites 1 through 7 in Fig. 7A–E respectively. While Fig. 7E depicts the heat cycles along the scanning direction, Fig. 7A to D depicts along the building directions. The highest temperature at point 1 never rose above 200 °C during the first two passes, and it stayed steady between 100° and 200 °C during the following passes. The starting temperature was just 600 °C at point 2, and it was roughly 850 °C at point 3 (see Fig. 7B and C). The subsequent thermal element at points 3, 4 and 5 were positioned roughly 0.5 mm below the weld pool. This was done to rectify the anomaly caused by placing it significantly away. When observing the cooling rates (seen in Fig. 7 (C and D)), the interval between the first two peaks were smaller than rest of the peaks, suggesting a rapid cooling phase in just printed layer. Larger time intervals in the subsequent peaks suggests slower cooling rates, signifying reduced downward conduction and radiation to the atmosphere. Such delays can significantly affect the print time;

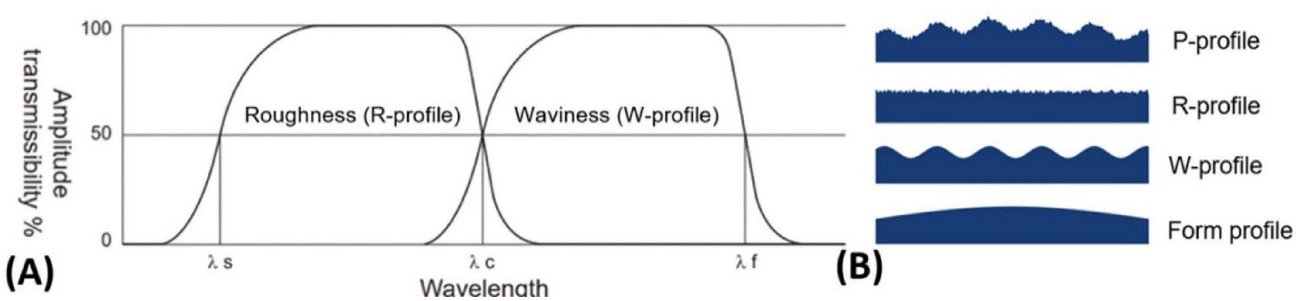

Fig. 6 Surface profiles-figures used with permission from Keyence Deutschland GmbH, **A** Definition of cut off wavelengths [34], **B** Profiles used to characterise a technical surface [36]

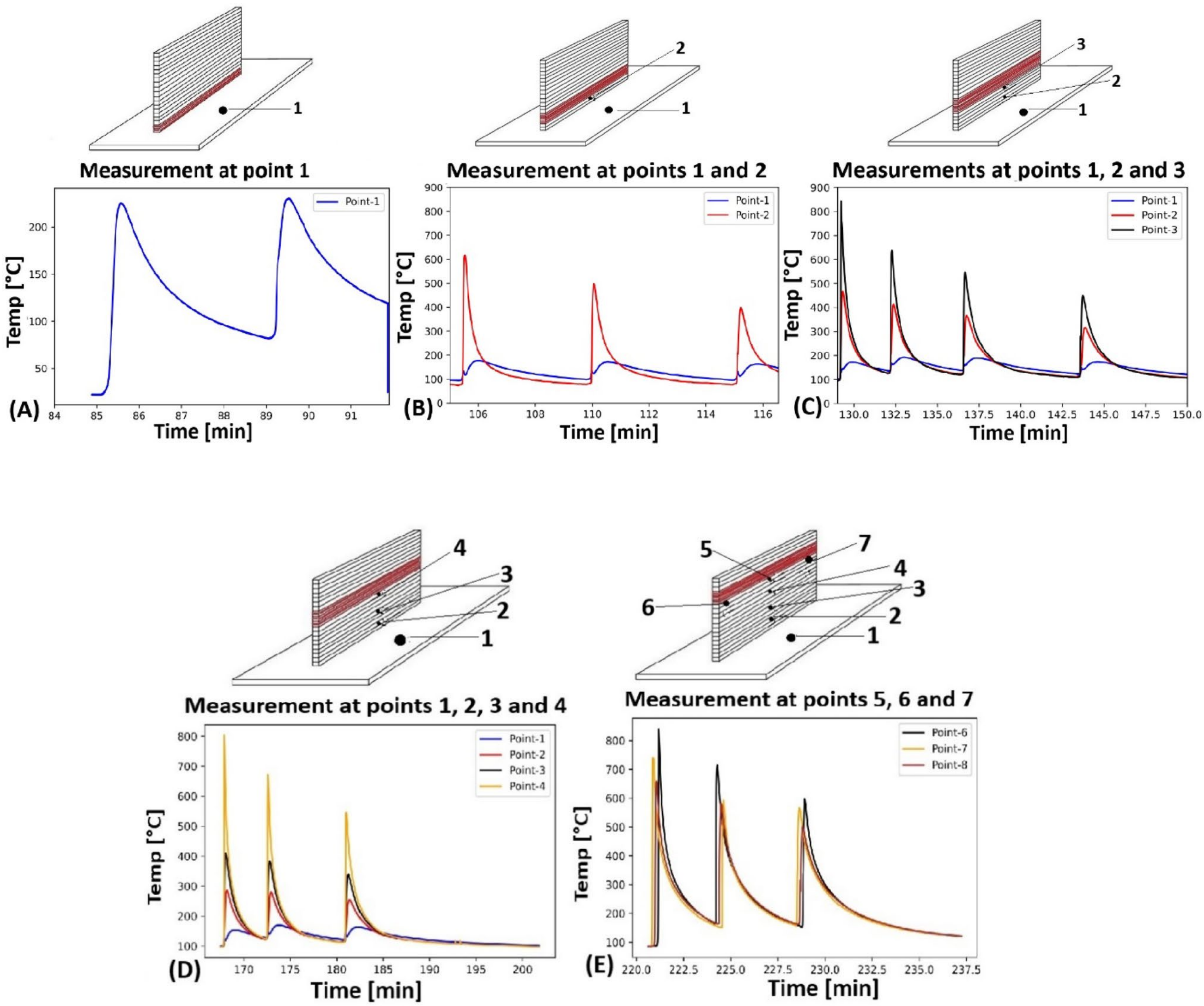

Fig. 7 The structure thermal cycles, **A** Thermal cycle when element at position 1, on substrate plate, **B** Thermal cycle recorded by two elements at positions 1 and 2, **C** Recorded at positions 1, 2 and 3, **D** Recorded at positions 1, 2, 3 and 4, and **E** Recorded at positions 5, 6 and 7

therefore, cooling strategies needs to be implemented. A similar methodology was adopted in [7], where a FLIR A655sc thermographic camera was used. It was observed that a steady state heat transfer was reached after the deposition of the first passes. The thermal evolution in the first deposited layer had a profound effect from the heat sink effect, which enables a faster cooling rate and reduced temperatures. A similar observation can be seen in the current study, where at point 1 during the deposition of first two layers, the temperature remained relatively stable at 250 °C at its peak and descended quickly. Similarly at points 5, 6 and 7 (Fig. 7E), temperature at point 5 had the maximum when compared to points 6 and 7, as seen in [7]. But the cooling rates seen here where slower when compared to [7], because a much larger waiting time was adopted and a starting temperature of 100 °C, as opposed to a waiting time of 15 s in [7]. Thus, by comparing both the studies, an appropriate cooling strategy needs to be devised to keep the temperature constant throughout the process.

Figure 8 shows an active melt pool observation being set up, where the first three images is an attempt to understand temperature gradients within a single layer as and when it was deposited, and the gradients are color-coded in Fig. 8D. To capture the weld pool, the camera was placed in such a way, that it could capture the entire bead length, this helped in understanding how quickly the temperature dropped once the torch has passed a particular position. When taking a closer look at Figs. 8A–C, a rapid cooling was seen in a single layer as the weld torch moved from right to left. For instance, in Fig. 8B, the temperature just below the torch was 1126 °C, and latter in Fig. 8C, it was 725 °C. That’s a quick drop of a 401 °C, such rapid cooling and re-melting

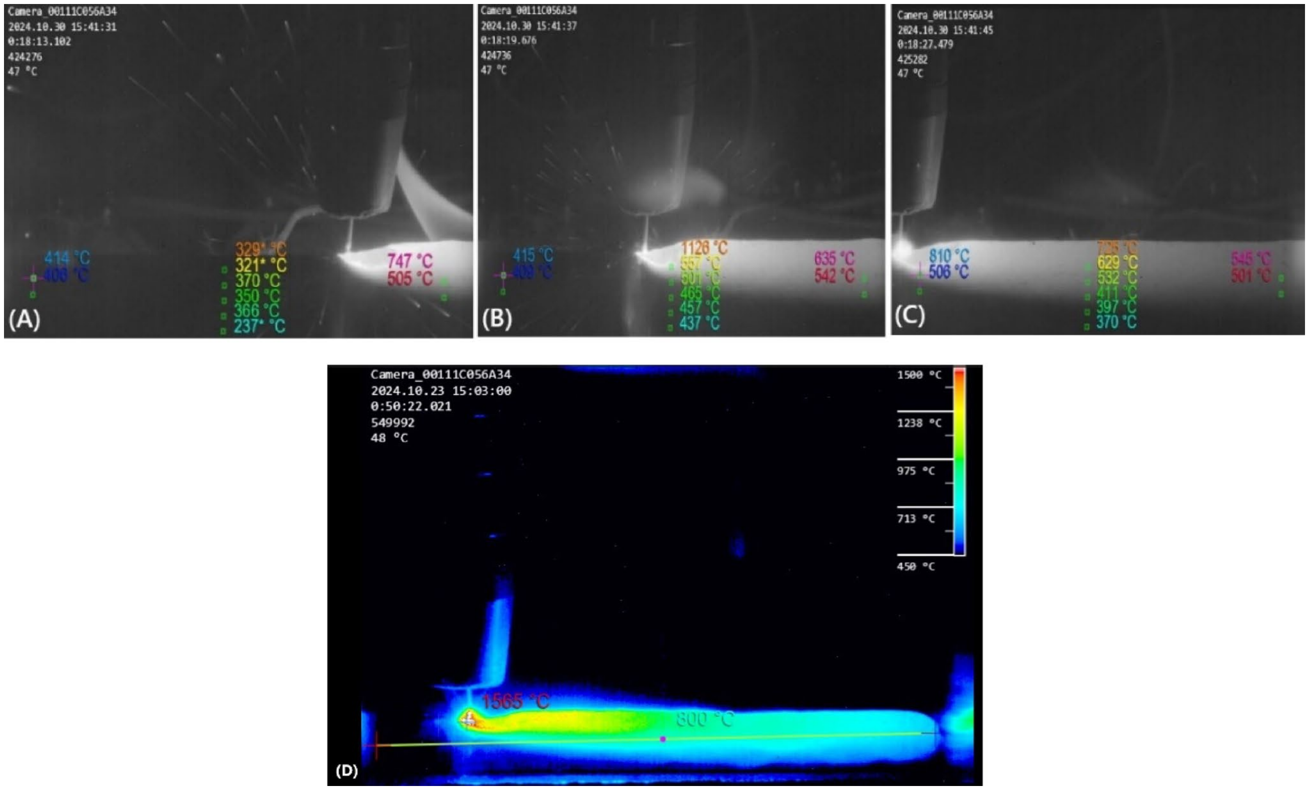

Fig. 8 Online monitoring of the weld pool. **A**–**C** Temperature recorded at different points and **D** Online monitoring of the weld pool

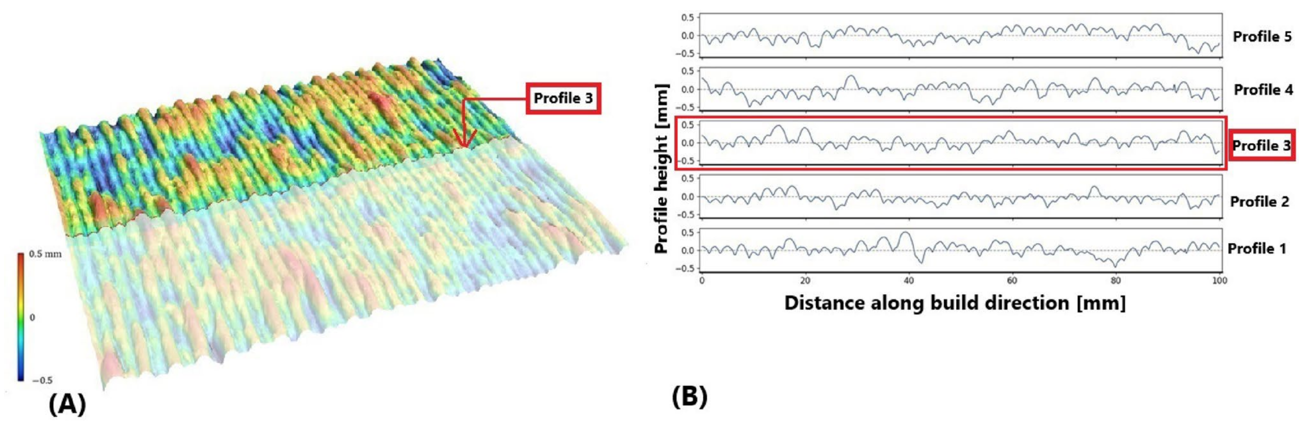

Fig. 9 Surface section of WAAM 316LSi thin walled structure showing **A** exaggerated topology map with 300% height and **B** evaluated profiles

has a profound effect on the grain structure growth, which is elaborated in Sect. 4.3. A closer look into the gradients (Fig. 8D) reveals the extend of the cooling rate seen in a single layer. While, at the point within the weld pool, the temperature was 1565 °C, whereas at the right end of the single layer, the maximum was approximately 713 °C. During fabrication of the walls, each layer was cooled down, and therefore the same layer is remelted when the next layer is deposited. Such scenarios enable the development of the non-uniform grain structures, which induces anisotropy within the structure [7, 37].

4.2 Surface characterisation results

Figure 9A, B displays the surface topology of the scanned 316LSi WAAM specimen. Five profiles were analysed using the scan approach described in Sect. 2.3, as shown in Fig. 9B.

Roughness was evaluated along the line profiles on the as-welded surface along the build direction using various iterations of λ_c as performed in related work [31]. However, this was found to be unsuitable for the sample due to the large discrepancies in roughness caused by notches at the layer boundaries, making R_z calculations of little meaning when following the recommendations in the ISO standards [34, 35]. Additionally, roughness measurements were also made along single layer ridges in the travel direction using $\lambda_c, l_r = 0.8$ mm and an evaluation length of 4 mm according to [35]. Although this yielded better results than in the build direction, the inhomogeneous nature of the unmachined surface caused discrepancies when assessing the R-profile metrics. For these reasons, The R-profile is disregarded in the further steps of characterization. The W-profile on the other hand, is the product of both deterministic features such as the layer boundaries and weld bead dimensions as well as random features caused by surface bulging and layer overlapping leading to error in the form of the WAAM structure. The cutoff wavelength λ_f is selected with the aim of isolating the W-profile—in this study defined as the deterministic waviness of the layers from the overall error in the form of the surface [34]. Following the similar methodology as Hensel et al. [31], this is investigated as a function of layer boundary height h, where h is determined by individually measuring the trough distances for each layer boundary along the five line-profiles. The layer boundary distribution can be seen in Fig. 10A, B, in which the average value is $h = 2.21$ mm with a standard deviation of 0.50 mm.

The waviness metrics W_z and W_a were evaluated using λ_f with four incrementations from h to $4h$, in which a comprehensive waviness evaluation is presented for the WAAM sample surface in the build direction. The h-factors were chosen as a range to observe the influence of changing λ_f on the resulting W-profile and Form-profile, and how this may be used to separate the deterministic and random surface features. The filtered W-profiles were generated through the Keyence VR-6000 software and processed in Python. Outliers are determined as values larger than 2.5 times the interquartile range (IQR). Each line profile is assessed separately as well as combined for each cutoff wavelength increment and is evaluated over the entire line profile length. Each cutoff wavelength is also equal to the sampling length, which is inversely proportional to the number of sampling lengths across the evaluation length. Figure 11C, D shows the result of calculating the W_z and W_a. Here, both metrics are seen to increase with a larger cutoff wavelength, with a substantial increase between $\lambda_f = h$ and $2h$. Using a cutoff of $\lambda_f = h$, the average layer boundary height is chosen as the cutoff wavelength. Although this results in a similar distribution of W_z and W_a for each profile, the sampling length does not always cover the distance of a complete layer boundary causing truncation and a loss of information for the layer waveforms, see Fig. 10D. Increasing λ_f to $2h$ solves this issue as the sampling length will always contain at least one complete layer. When increasing λ_f to $3h$ and $4h$ however, the distributions become less regular as well as including more outlier values for both W_z and W_a. This is because by increasing the cutoff wavelength, more error from the overall form of the surface is included in the W-profile, thus detracting from the desired characterization of the deterministic features of the WAAM sample. $2h$ is therefore chosen as a suitable upper cutoff, see Fig. 11A, B.

4.3 Microstructural characterisations

Figure 12A shows a visual representation of the sample directions along which the microstructure was checked. Figure 12B shows the XY-plane, where the red box indicates the point of interest within this structure. The evolution is further enlarged in Fig. 12C, where a gradual shift to columnar grain structure is seen from the fusion line (seen both in Fig. 12B and C as dark patches). While closely observing Fig. 12C, a mixture of a lathy delta (δ) ferrite and skeletal ferrite (both black in colour) is seen within the background

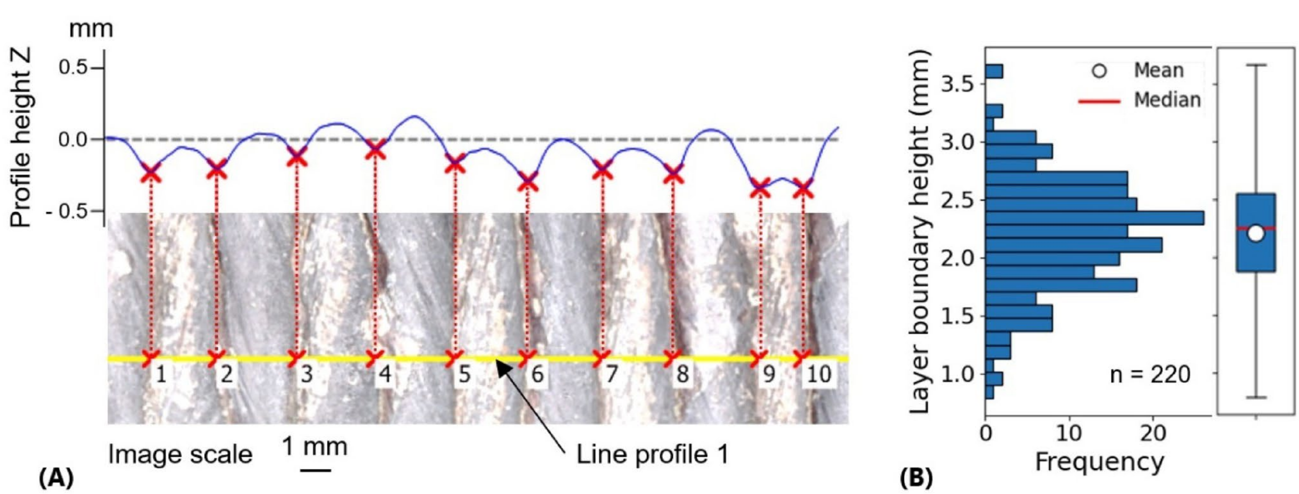

Fig. 10 **A** First 10 troughs along the line profile 1 illustrating layer boundary height measurements and **B** Results distribution for layer boundary heights for all line profiles

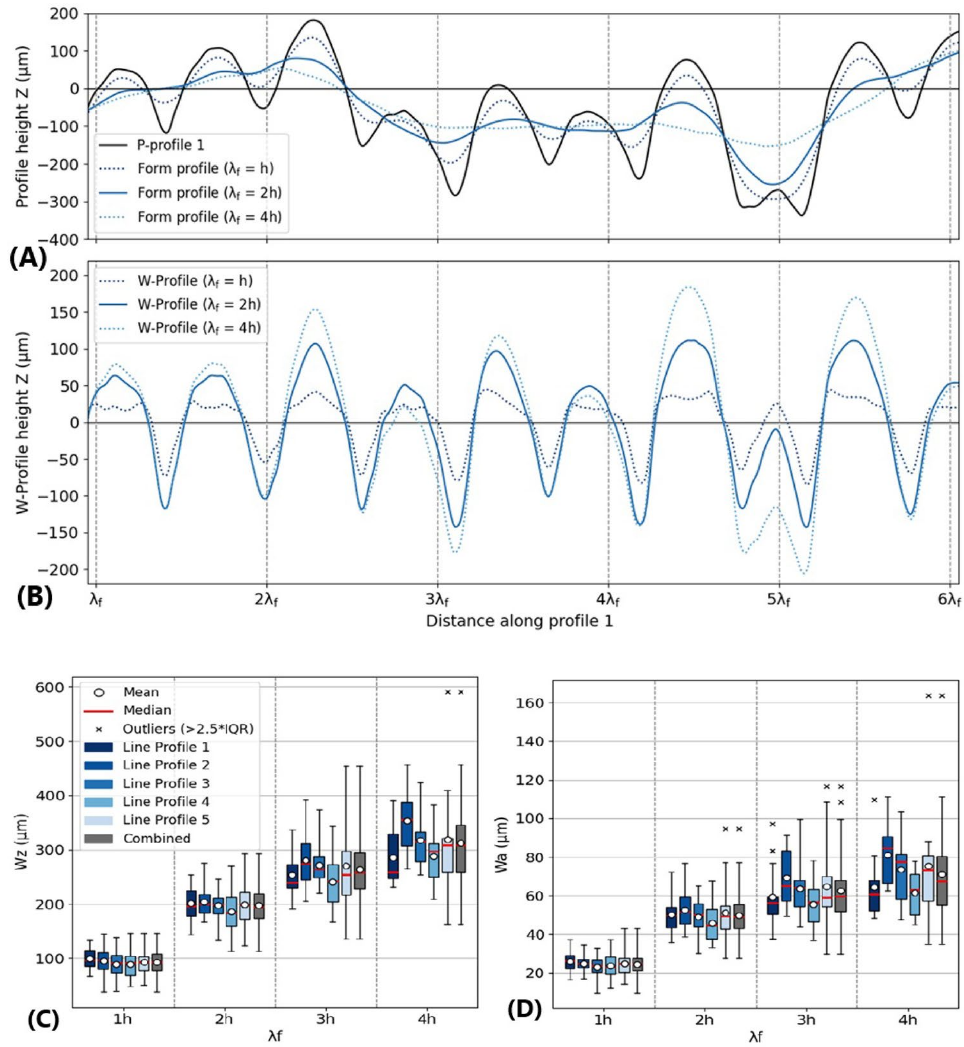

Fig. 11 **A** Section of P-profile showing results of applying different cut-off filters λ_f to get error of form profiles, **B** Resulting W-profiles after application of cut-off filters, **C,D** Box and whisker plots showing distribution of W_Z and W_a across iterations of λ_f respectively

of an austenite (γ) matrix [7, 37, 41]. Therefore, there is a distinct γ/δ interface seen in the structure with austenite dendrites growing in the building direction.

Figure 13A and B illustrates the microstructure in the YZ-plane, where a clear boundary between two adjacent layers are visible. The diffusion zone is marked by a transition from lathy ferrite to a skeleton ferrite. Just below the diffusion zone (i.e. upper region of a single layer) is characterised by the presence of lathy ferrites, while the lower regions of the layer by the skeleton ferrite. Whereas the diffusion zone itself exhibits a strip morphology with negligible secondary dendrite arm [51]. In the diffusion zone, the austenite dendrites growth is perpendicular (see Fig. 13C-marked as red and blue), such an observation was also reported in other studies [7, 37, 51]. The ferrites exhibited a narrow granular morphology (shown as blue in Fig. 13C), whereas the same showed a coarser lathy structure in the region marked as red. In the regions marked as green, the ferrites with both skeletal and lathy morphologies can be seen. Such transitions seen can be attributed to the cooling gradients seen within each layer. While deposition of each layer, a wait time of appox. 5–7 min was adopted and during this time the layers where air-cooled to 50 °C. Figure 13D shows the microstructure in XZ-plane, and as stated earlier the melting-solidification cycle induces an equiaxial-columnar-equiaxial structure. The process is repeated throughout the manufacturing process leading to the formation of such periodic microstructural bands along the direction of deposition [7].

The presence of δ-ferrite distributed within an austenite matrix for an austenitic stainless steel is not unusual during WAAM process. Such a distribution is attributed to the conditions of solidification and cooling rates. Four possible ways of solidification and transformation can be thought of in the case of austenitic stainless steel namely: solidification types A (austenite) and AF (austenite-ferrite), related to austenitic solidification as the first phase, whereas types FA (ferrite–austenite) and F (δ-ferrite) have ferrite as the primary phase, further detailed information can be found in [37–41]. In the case of 316LSi (currently used in this study),

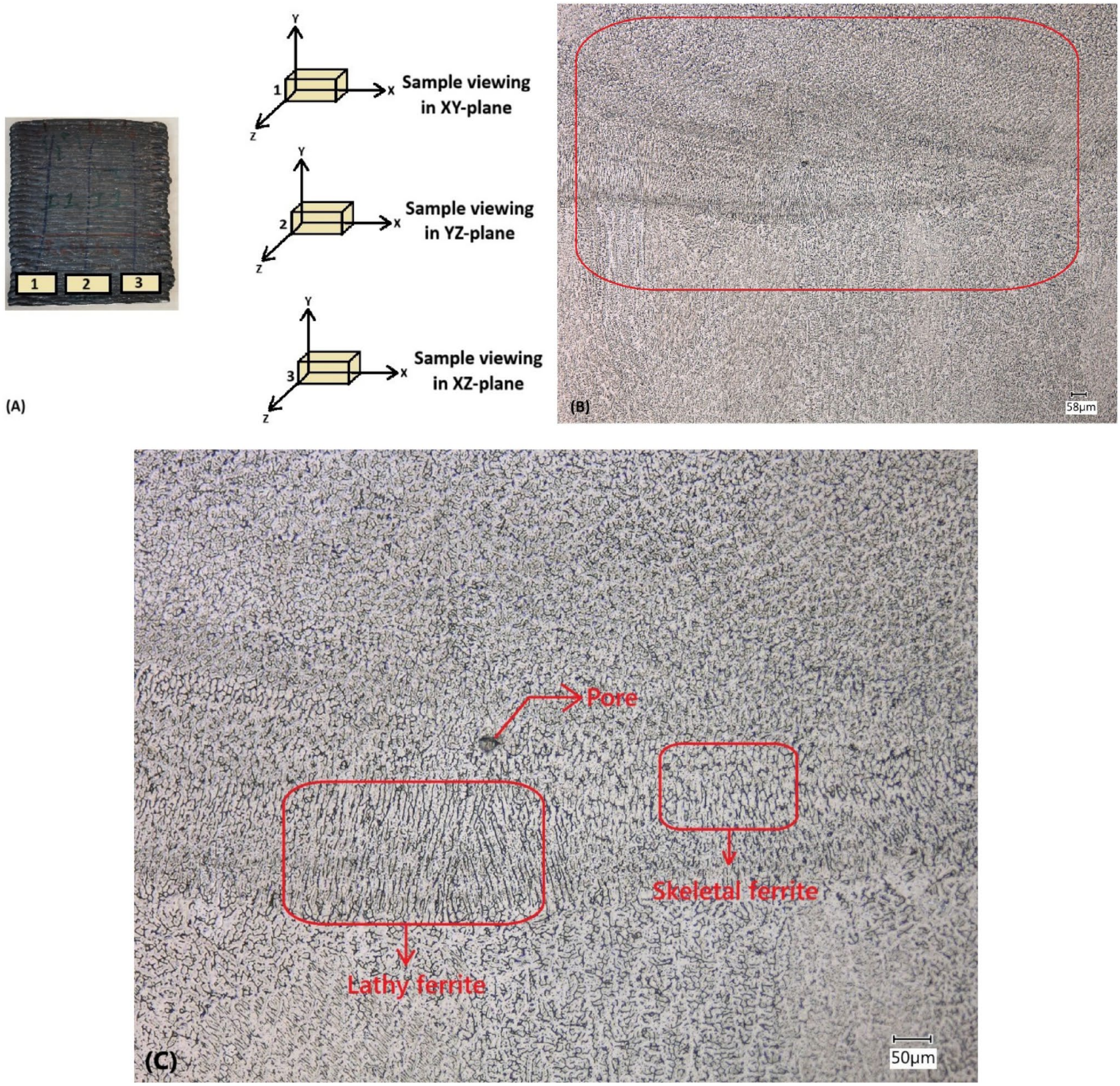

Fig. 12 **A** Region where microstructure was studies, **B** A typical diffusion zone seen in XY-plane and **C** An enlarged image within the diffusion zone

the solidification phase observed is FA, which has a transformation as illustrated below;

$$\mathrm{L} \rightarrow \mathrm{L} + \delta \rightarrow \mathrm{L} + \delta + (\delta + \gamma)_{\mathrm{per-eut}} \rightarrow \delta + \gamma \tag{3}$$

where the microstructural composition is usually a mix of skeletal or lathy δ-ferrite in a predominantly austenitic matrix (see Figs. 12 and 13). Therefore, high cooling rates evident in Figs. 7 and 8 doesn't allow a clear and complete transformation from δ-ferrite to austenite, thereby retaining the primary δ-ferrite within the melt zone [37–41].

The thermal gradients from Fig. 7C along with the resulting microstructure is shown in below in Fig. 14A, B. The formation of long columnar austenitic grains is primarily driven by the strong thermal gradients and layer-wise heat accumulation inherent in the process [42]. At lower regions of the build, rapid heat extraction through the substrate produces high thermal gradient (2 min seen in Fig. 14) and fast solidification. Such higher gradients enable the formation of δ-ferrite in lower regions of the structure [41], also corroborated by the ferrite content seen in Fig. 17A. In addition to the formation of δ-ferrite, such solidification rates promotes

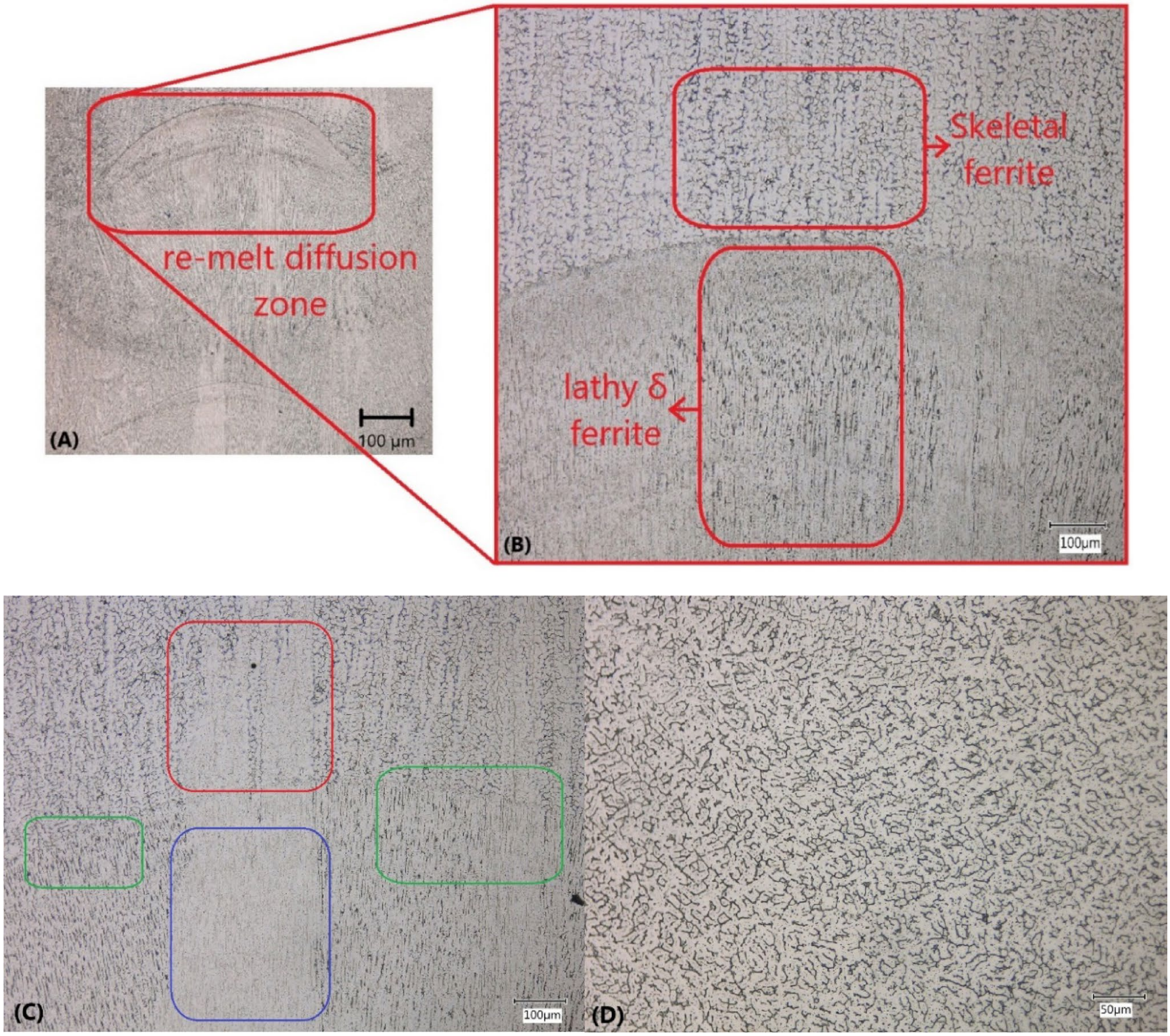

Fig. 13 **A** An image from YZ-plane, **B** An enlarged region within the diffusion zone with ferrite and pearlite regions, **C** Microstructure along the XZ-plane with its Acicular ferrite and pearlite formations, and **D** Microstructure in XZ-plane

epitaxial grain growth from the fusion boundary and stabilizes the development of elongated grains (seen as yellow coloured in Fig. 14) aligned with the build direction[43]. As the deposition of the subsequent layers progresses, repeated re-heating of underlying layers progressively reduces the cooling rate in the upper regions, creating a more uniform and slower solidification environment. The sustained thermal gradients, combined with decreasing cooling rates, allows previously established columnar grains to extend continuously upward from layer to layer, producing grains that may span multiple deposited beads [44, 45]. Lower cooling rates also lead to dendrite AF structure [41], which can be seen within the yellow columnar grains in Fig. 14B. Thus, these columnar grains are not featureless structures, but are composed of well defined dendritic structure. As the melt solidifies under a high thermal gradient, each elongated columnar grain grows through the advancement of primary dendrite arms aligned with the heat-flow direction, while secondary arms branch laterally within the same crystallographic orientation. These dendrite arms form the cellular-dendrite arms from the cellular-dendrite pattern characteristic of austenitic stainless steel solidification and exist entirely within individual columnar grains, providing fine-scale morphology that accompanies the coarse, directionally solidified grain structure [46, 47]. The next section will further extend the effect of these grain structure on to the mechanical properties in terms of tensile and hardness tests respectively.

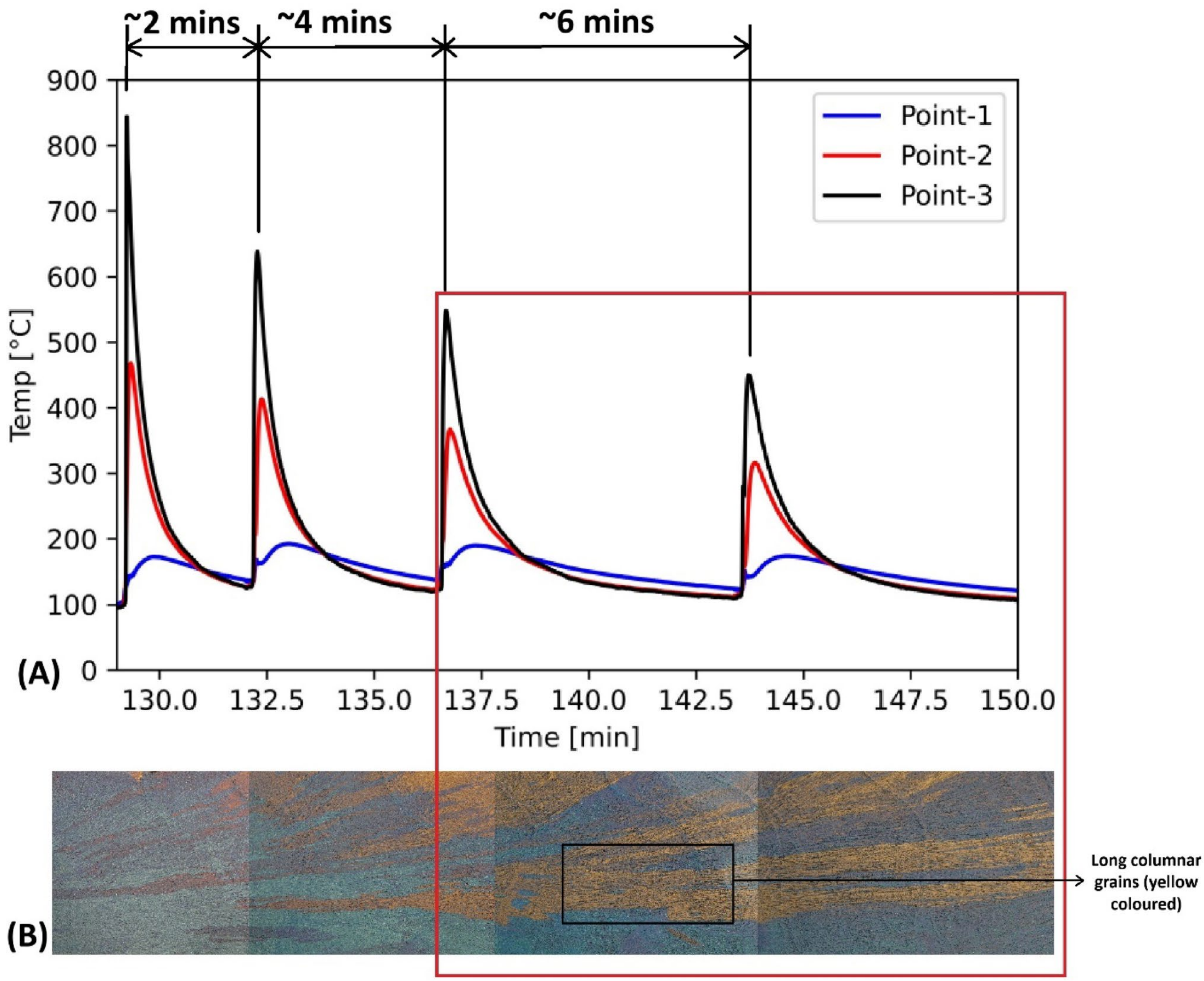

Fig. 14 **A** The structure thermal cycles recorded at positions 1, 2 and 3. **B** Microstructure seen in the YZ-plane

4.4 Mechanical characterisations

Figure 15A and B shows the tensile test plots from WAAM [0°] and [90°] samples respectively, and for all the samples, the yield strength calculated at 0.2% proof strain (Rp0.2), ultimate tensile strength (Rm), and fracture strain (ε_f) were ascertained. And these properties with its respective comparisons with a non-WAAM samples (wrought) are shown in Fig. 15C–E respectively. From Fig. 15A, B, it's clear that regardless of the orientations, the material exhibited non-linear behaviour with both elastic and plastic deformations present before final failure [7]. When Rp0.2 was compared with respect to wrought samples, WAAM [0°] exhibited higher yield strengths where the percentage increase was approximately 31% (average approximation, Fig. 15D). While on a percentile scale being lower than the former, [90°] samples too exhibited higher Rp0.2. Such directionally dependent properties were seen in other studies and are elaborated in Table 4. But in [7] a variation in properties were seen in samples that were as built and those milled. Milled samples exhibited higher Rp0.2 when compared to non-milled samples which can be attributed to the notch effect[32]. Such increments were seen in samples from other orientations [such as 0°, 45° and 90°], and these increments were of the order approx. 1.2 times.

Ultimate strengths Rm with respect to wrought samples were seen to be higher in the case of WAAM [0°]. But WAAM [90°] was seen to have similar Rm as those of the wrought ones. Here too, as reported in [7] the properties were directional to the deposition direction. The anisotropy seen here wasn't seen in [37] where the same was noticed in as-built samples. Finally, the fracture strain seen in wrought samples were comparably higher when compared to WAAM samples. On a percentile scale this was approximately 45% higher. Elsewhere, the strains were seen to be similar and were in general agreement as seen here

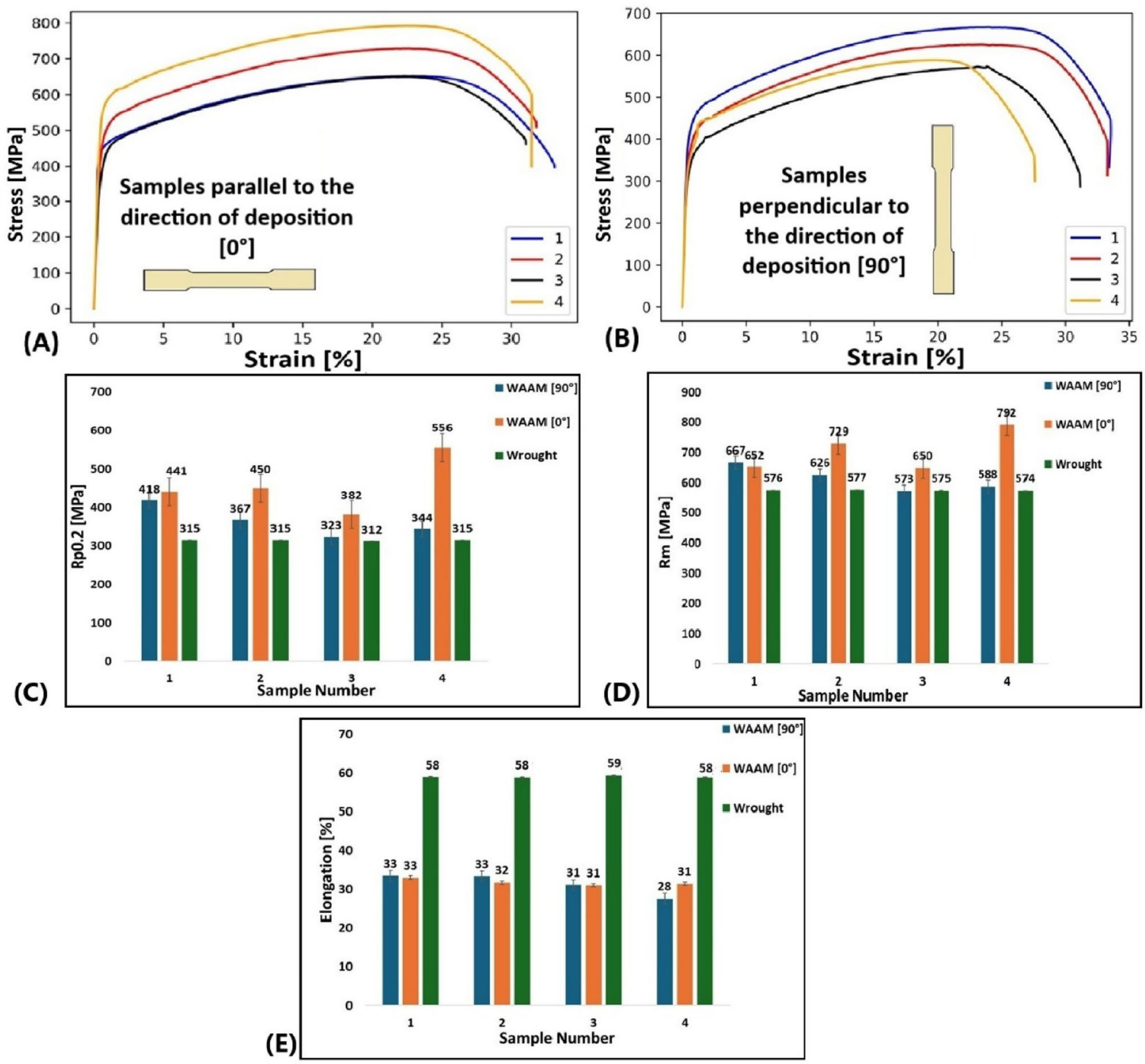

Fig. 15 Mechanical tests results. **A** Stress–strain curve from WAAM [0°], **B** Stress–strain curve from WAAM [90°], **C** Rp0.2 comparisons between samples **D** Rm comparison between samples and **E** Elongation comparison between samples

Table 4 A comparison of Rp0.2 and Rm from other authors

Author's	Welding source	Rp0.2 [MPa]	Rm [MPa]
Chen et al. [49]	GMAW	235	533
Wang et al. [50]	GMAW	418	553
Wang et al. [51]	CMT	377 (average)	558 (average)
Kannan et al. [52]	GMAW	311	589
Xie et al. [53]	CMT	250 approx	550 approx
Rodriguez et al. [24]	CMT	351 (average)	568 (average)
Wu et al. [54]	GMAW	338 (average)	483 (average)
Ye et al. [55]	CMT	333 (average)	576 (average)
Moore et al. [56]	GMAW	304–312	580 approx
Andrade et al. [7]	CMT	409 (average)	686 (average)
Current work	CMT	457 (average)	705 (average)

[7, 37]. The observed reduction in failure strain in WAAM samples compared to wrought samples is notable, despite both being based on an austenitic matrix. This difference is likely influenced by the evolution of the WAAM microstructure, which was discussed in the previous section. WAAM samples (from 316LSi) commonly exhibit a mixture of austenite (γ-phase, face-centred cubic, FCC) and δ-ferrite (body-centred cubic, BCC). While, austenite's FCC structure provides higher ductility due to multiple slip system, δ-ferrite's BCC structure is generally stronger but less ductile at room temperature. The heterogenous distribution of these phases in WAAM structures may therefore contribute

to localized differences in properties including failure strain, potentially even reducing the latter when compared to fully austenitic wrought samples. Further experimental investigation is needed to establish a definitive correlation between phase distribution and mechanical performance in WAAM 316LSi.

The WAAM samples in this work tends to be less tough when compared to wrought samples, but strength wise seems to perform better. As a result, the optimum parameters obtained from the ML model estimated in [28] were able to provide a structure with ideal mechanical characteristics. The results from other articles are shown in Table 4 and comparisons made with the results obtained in this study. From Table 4, its clear that the Rp0.2 varies from as low as 235 MPa to as high as 457 MPa, and Rm between 480 to 700 MPa. Such scatter in values seems to stem from several factors, and the authors have used different power sources during the WAAM process. The values obtained in the current study seems to agree with most of the other findings. In addition to these, the values obtained in the current study are superior to the values of 320 MPa (Rp0.2), 510 MPa (Rm) and 25% (ε_f) stated in EN ISO 14343 [48] for 316LSi feed material.

Figure 16 presents the hardness distribution along the strip extracted from WAAM plate_2 (Fig. 5), measured to assess the homogeneity of material properties throughout the build. The tests were carried out along the YZ-plane, where hardness indentations were performed every 5 mm along the strip length, revealing a base hardness of 173 HV, with values oscillating between 185 and 195 HV along the mid-height. Occasional peaks reaching 207 HV were observed, which can plausibly be attributed to local thermal gradients and variable cooling behaviour during deposition [7, 57]. The Vickers HV30 scale was selected for this analysis to obtain a representative bulk hardness value across the heterogeneous WAAM microstructure. WAAM-deposited 316LSi typically exhibits coarse, directionally solidified austenite with lathy or skeletal δ-ferrite, and larger Vickers load (HV10-HV30) are widely used in WAAM and welded stainless steels to average out local microstructural variability and reduce indentation-to-indentation scatter. This choice aligns with established practise in WAAM hardness characterisation [58, 59] and with ASTM E384 [60] guidance on selecting an indentation load appropriate for coarse or multiple microstructures.

The presence of δ-ferrite was explained in Sect. 4.3, but a quantification and its distribution within a sample might

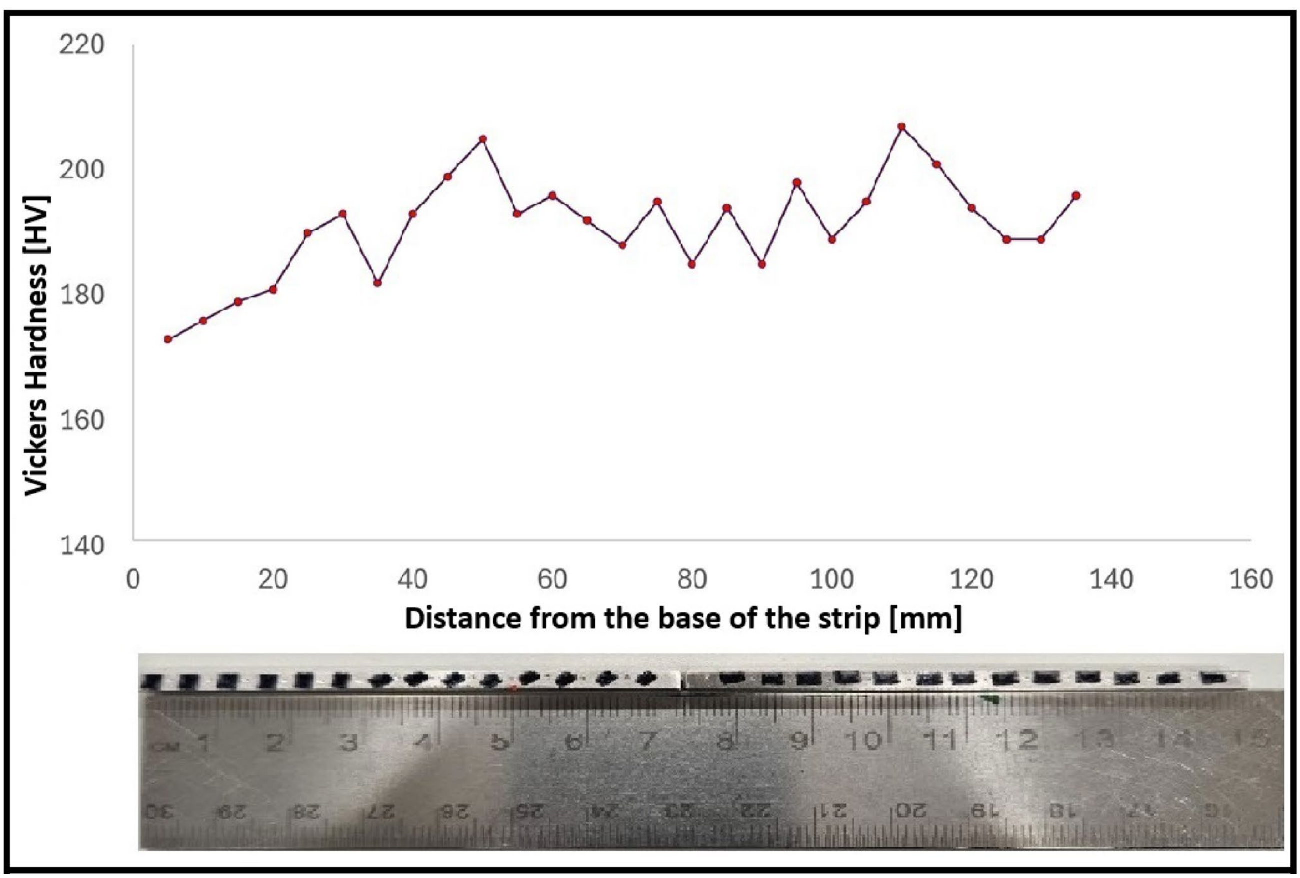

Fig. 16 Hardness distribution along the length of the strip from the base

help to understand the mechanical properties of the samples seen previously in Fig. 15. During the normal cooling phase, in a ferrite–austenite transformation the δ-ferrite phase transforms continuously into the γ-austenite phase through solid-state transformation. But, during WAAM process of 316LSi, the rapid cooling limits the transformation of the whole δ to γ, therefore a significant amount of δ stays in an overwhelming γ matrix. To estimate the amount of δ-ferrite within the structure, a fertiscope was used. The estimation was carried out based on a methodology established by Jafarzad-Shaya et al. [61], wherein the ferrite content was measured in the bottom, middle and upper regions of the structure. Figure 17A illustrates the ferrite content in samples from Fig. 15B. The regions of interest are highlighted in the left corner of the plots. The lower and middle regions of the sample had higher ferrite content when compared to the higher regions. The higher ferrite content in the lower regions is due to the higher cooling rate, resulting from the short distance from the substrate plate. On the other hand, lower ferrite content in the upper regions is due to lower cooling rate caused by increased heat accumulation and reduced conductive flux. A closer look into the middle regions of the sample, approximately corresponding to the gauge length (35 mm) reveals a plausible link to increase in Rp0.2 and Rm to the higher ferrite content in the samples observed in these regions. δ-ferrite plays a significant role in strengthening the structure primarily through two mechanisms. Firstly, it acts a reinforcing second phase and secondly, due to its incompatibility with austenite, GNDs (geometrically necessary dislocations) accumulate at the interface between the ferrites and the austenite phase respectively. In addition to these two mechanisms the low stacking fault energy can facilitate dislocation pile-ups by limiting cross-slips [62–64]. Finally, there is the general characteristic associated with a face centred cubic structure (FCC) of an austenite steel and body centred structure (BCC) of ferrites, where the former has lower yield strengths and higher ductility, while the latter has higher yield strengths but lower ductility [65]. Figure 17B illustrates the presence of the ferrites (black in colour) within an austenite matrix, between two fusion zones marked as red. Since, these dual phases are retained within the micro-structure, 316LSi structure post WAAM processes tends to exhibit a dual-phase, harmonic, and periodic structure [61].

5 Conclusions

This study demonstrated in-situ melt pool temperatures and cooling rates during CMT-WAAM fabrication of walled structures. The consequences of the temperature gradients on surface morphology, microstructure, and mechanical properties were examined, leading to the following conclusions.

- Temperature measurements revealed substrate temperature remained below 300 °C, while peak temperatures during layer deposition did not exceed 850 °C. Cooling durations of 4–7 min under natural air cooling reflected strong thermal gradients along the build height. HDR imaging confirmed downward heat conduction and rapid cooling of newly deposited layers, validating the non-uniform thermal history measured by the thermocouple.
- The microstructure exhibited a predominantly austenitic matrix containing lathy and skeletal δ-ferrite, consistent with the ferritic-austenitic solidification and subsequent thermal cycling observed in this study. The δ-ferrite morphology remained largely lathy and skeletal throughout the build, reflecting the influence of local cooling conditions and thermal gradients on phase formation.
- Surface quality was assessed for the as-welded structure, finding that the waviness profile can be split into deterministic and random features by choosing the cut-off frequency λ_f of 2 h. This resulted in Wz of 197.9 µm and Wa of 49.8 µm for the deterministic features. Furthermore, it was found the ISO standards were not effective in characterizing roughness in the build direction.
- Mechanical testing revealed a clear anisotropy in the WAAM samples, which can plausibly be linked to the directionally solidified microstructure developed during deposition. Tensile samples extracted parallel to the build direction [0°] showed ~31% increase in Rp0.2 and corresponding higher Rm values relative to wrought samples, whereas perpendicular samples [90°] exhibited strengths similar to wrought samples. The observed anisotropy can be linked to the presence of δ-ferrite within an austenitic matrix.
- Finally, the presence of ferrite in the structure was quantified which showed a varied presence within the structure. The lower and middle regions of the sample had higher concentration of ferrite when compared to the upper regions. The presence of the ferrite in a predominantly austenitic microstructure affected the mechanical properties. Thus, the toughness was nearly halved when compared to normal 316LSi steel, whereas an increase in Rp0.2 and Rm was observed.

Thus, the study provides an insight into various aspects of 316LSi when used as a feedstock material during WAAM. Although previous research conducted in-depth analyses of the microstructure evolution and demonstrated the obvious presence of ferrites, the latter's impact on mechanical characteristics has received less attention. As a result, the current study made an effort to comprehend the effect of ferrites

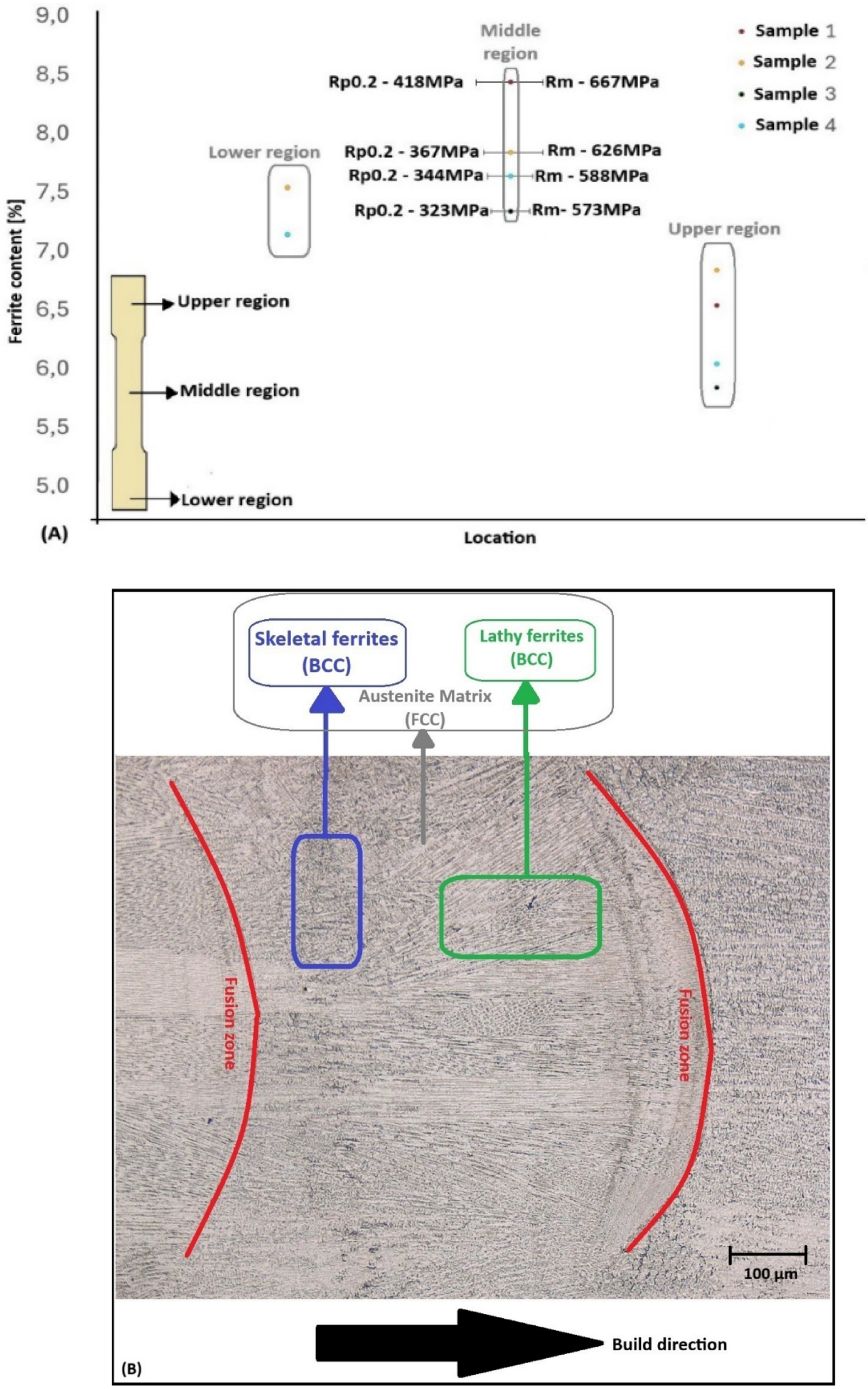

Fig. 17 **A** Percentage composition of ferrite content in the samples, and **B** Optical micrograph showing the ferrite distribution (skeletal and delta) between two fusion zones

on the mechanical properties, which is crucial, particularly when used in structural applications. It is clear that there is need for more research into the relationship between the evolution of the microstructure and the resulting mechanical characteristics, as well as new WAAM techniques/strategies to customize the properties according to the needs of the application.

Acknowledgements Acknowledgments Ms. Andrea Hasselmann, Mr. Andreas Gobbert, Mr. Sven Trapp and Mr. Thomas Hilbrecht, University of Applied Science Hamburg, Institute of Material Science and Joining, Berliner Tor 13, D-20099, Germany.

Author contribution S.P.S: Conceptualization; writing-original draft; methodology; validation; visualisation; data curation. K.F.T.V: Investigation; validation; software; formal analysis; data curation; writing-original draft. E.M: Project administration; data-curation. S.A: software; data curation. R.S: software; data curation. C.K.F: Project management; funding acquisition; Resources; writing-review. M.B: Project management; funding acquisition; Resources; writing-review and editing; Supervision. S.S: Conceptualization; funding acquisition; methodology; project management; writing-review and editing; resources; supervision; validation.

Funding Open Access funding enabled and organized by Projekt DEAL. The work was performed within the research project Layer – "Lebensdauersteigerung von additive gefertigten (WAAM) Bauteilen mittels hybrider Fertigungsverfahren", funded by the German Federal Ministry for Economic Affairs and Climate Action (project number 03SX592), with nine co-operative partners, namely Mecklenburger Metallguss GmbH, MEYER WERFT GmbH & Co. KG, Laser cladding Germany GmbH, FEM-Composites GmbH, Ing. Grimm Schweißtechnik GmbH, HiFIT Vertriebs GmbH, KARSTENS WATERCUT & WELDING, TRIMET Aluminium SE, Deutsches Zentrum für Luft- und Raumfahrt (DLR) e.V.-Institut für Maritime Energiesystem.

Data availability No datasets were generated or analysed during the current study.

Declarations

Competing Interests The authors declare no competing interests.

References

1. Rodrigues AT, Duarte V, Miranda RM, Santos TG, Oliveira JP (2019) Current status and perspectives on wire arc additive manufacturing (WAAM). Materials. https://doi.org/10.3390/ma12071121
2. Ding D, Pan Z, Cuiuri D, Li H (2015) Wire-feed additive manufacturing of metal components: technologies, developments and future interests. Int J Adv Manuf Technol 81:465–481
3. Müller J et al (2019) Design and parameter identification of wire and arc additively manufactured (WAAM) steel bars for use in construction. Metals 9(7):725. https://doi.org/10.3390/met9070725
4. Wynne Z et al (2022) Dynamic testing and analysis of the world's first metal 3D printed bridge. Case Stud Constr Mater 17:e01541. https://doi.org/10.1016/j.cscm.2022.e01541
5. Greer C et al (2019) Introduction to the design rules for metal big area additive manufacturing. Addit Manuf 27:159–166. https://doi.org/10.1016/j.addma.2019.02.016
6. Ma G, Zhao G, Li Z, Yang M, Xiao W (2019) Optimization strategies for robotic additive and subtractive manufacturing of large and high thin-walled aluminium structures. Int J Adv Manuf Tech 101:1275–1292. https://doi.org/10.1007/s00170-018-3009-3
7. Andrade DG et al (2024) Mechanical properties of 3D printed CMT-WAAM 315 LSi stainless steel walls. J Const Steel Res 215:108527. https://doi.org/10.1016/j.jcsr.2024.108527
8. Stainless Steel in Figures, World Stainl. Assoc, 2022. https://www.worldstainless.org/files/issf/non-image-files/PDF/Stainless_Steel_in_Figures_2022_public_English.pdf. Accessed 13 Oct 2022
9. Long J et al (2022) High-power wire arc additive manufacturing of stainless steel with active heat management. Sci Technol Weld Join. https://doi.org/10.1080/13621718.2022.2045127
10. Chen X, Li J, Cheng X, He B, Wang H, Huang Z (2017) Microstructure and mechanical properties of the austenitic stainless steel 316L fabricated by gas metal arc additive manufacturing. Mater Sci Eng A 703(4):567–577. https://doi.org/10.1016/jmsea.2017.05.024
11. Xu F, Dhokia V, Colegrove P, McAndrew A, Williams S, Henstridge A, Newman ST (2018) Realisation of a multi-sensor framework for process monitoring of the wire arc additivemanufacturing in producing Ti-6Al-4V parts. Int J Comput Integr Manuf 31(8):785–798
12. Rios S, Colegrove PA, Martina F, Williams SW (2018) Analytical process model for wire+arc additive manufacturing. Addit Manuf 21:651–657. https://doi.org/10.1016/j.addma.2018.04.003
13. Saeed G, Lou M, Zhang YM (2004) Computation of 3D weld pool surface from the slope field and point tracking of laser beams. Meas Sci Technol 15:389. https://doi.org/10.1088/0957-0233/15/2/012
14. Richter A, Gehling T, Kai T, Wesling V, Rembe C (2021) Real-time measurement of temperature and volume of the weld pool in wire-arc additive manufacturing. Meas Sens 17:1000602. https://doi.org/10.1016/j.measen.2021.100060
15. Li T, Cao Y, Zhang Y (2024) Analysis of weld pool region constituents in GMAW for dynamic reconstruction through characteristic enhancement and LSTM U-Net networks. J Manuf Process 127(15):573–588. https://doi.org/10.1016/j.jmapro.2024.07.084
16. da Silva LJ, Souza DM, de Araujo DB, Reis RP, Scotti A (2020) Concept and validation of an active cooling technique to mitigate heat accumulation in WAAM. Int J Adv Manuf Technol 107:2513–2523. https://doi.org/10.1007/s00170-020-05201-4
17. Wu B, Pan Z, Ding D, Cuiuri D, Li H, Fei Z (2018) The effects of forced interpass cooling on the material properties of wire arc additively manufactured Ti6Al4V alloy. J Mater Process Technol 258:97–105. https://doi.org/10.1016/j.jmatprotec.2018.03.024

18. Zhang Z, Yan J, Lu X, Zhang T, Wang H (2023) Optimization of porosity and surface roughness of CMT-P wire arc additive manufacturing of AA2024 using response surface methodology and NSGA-II. J Mat Res Tech 24:6923–6941. https://doi.org/10.1016/j.jmrt.2023.04.259
19. Xiong J, Li Y, Yin Z, Chen H (2018) Determination of surface roughness in wire and arc additive manufacturing based on laser vision sensing. Chin J Mech Eng 31(74):6851. https://doi.org/10.1186/s10033-018-0276-8
20. Aris NFM, Cheng K (2008) Characterization of the surface functionality on precision machined engineering surfaces. Int J Adv Manuf Technol 38:402–409. https://doi.org/10.1007/s00170-007-1340-1
21. Cheng J, De Waele W (2024) Prediction and optimization of surface waviness of WAAM components using a hybrid rank-gaussian PSO algorithm and ANN. Structures 69:107247. https://doi.org/10.1016/j.istruc.2024.107247
22. Albannai AI, Ramirez AJ (2024) The effect of altering heat input & torch motion on the grain formation of SS316L material in WAAM. Discover Mech Eng 3(1):49. https://doi.org/10.1007/s44245-024-00082-3
23. Xu H, Tian T, Hua B et al (2023) Effect of in-situ rolling and heat treatment on microstructure, mechanical and corrosion behaviours of wire-arc additively manufactured 316L stainless steel. J Mater Res Technol 27:3349–3361. https://doi.org/10.1016/j.jmrt.2023.10.168
24. Rodriguez N, Vasquez L, Huarte I, Arruti E, Tabernero I, Alvarez P (2018) Wire and arc additive manufacturing: a comparison between CMT and TopTig processes applied to stainless steel. Weld World 62:1083–1096. https://doi.org/10.1007/s40194-018-0606-6
25. Wu W, Xue J, Wang L, Zhang Z, Hu Y, Dong C (2019) Forming process, microstructure, and mechanical properties of thin-walled 316L stainless steel using speed-cold-welding additive manufacturing. Metal 981(1):109. https://doi.org/10.3390/met9010109
26. Tabernero I, Paskual A, Alvarez P, Suarez A (2018) Study on arc welding processes for high deposition rate additive manufacturing. Procedia CIRP 68:358–362. https://doi.org/10.1016/j.procir.2017.12.095
27. Prado-Cerqueira JL et al (2018) Analysis of favourable process conditions for the manufacturing of thin-wall pieces of mild steel obtained by wire and arc additive manufacturing. Materials 11(8):1449. https://doi.org/10.3390/ma11081449
28. Subadra SP, Mayer E, Wachtel P, Sheikhi S (2024) Feasibility study on machine learning methods for prediction of process-related parameters during WAAM process using SS-316L filler material. Weld World 68:3205–3214. https://doi.org/10.1007/s40194-024-01855-w
29. ISO-6892-1 (2009) Metallic materials-tensile testing-part 1: methods of test at room temperature
30. DIN EN ISO 6507-1:2018-07 (2018) Metallische Werkstoff-Härteprüfung nach Vickers-Teil 1: Prüfverfahren (ISO 6507-1:2018); Desutsche Fassung EN ISO 6507-1
31. Hensel J, Przyklenk A, Müller J, Köhler M, Dilger K (2022) Surface quality parameters for structural components manufactured by DED-arc processes. Mater Des 215:110438. https://doi.org/10.1016/j.matdes.2022.110438
32. Nafar Dastgerdi J, Jaberi O, Hensel J (2025) Characterization of surface irregularities and fatigue strength evaluation of wire arc additive manufactured high strength steel specimens. Int J Fatigue 192:108737. https://doi.org/10.1016/j.ijfatigue.2024.108737
33. Xiong J, Li YJ, Yin ZQ, Chen H (2018) Determination of surface roughness in wire and arc additive manufacturing based on laser vision sensing. Chin J Mech Eng 31:1–7
34. DIN EN ISO 4287: 2010-07 Geometrical Product Specifications (GPS) - Surface texture: Profile method - Terms, definitions and surface texture parameters, Deutsches Institut für Normung
35. DIN EN ISO 4288: 1998-04 Geometrical product specification (GPS)-Surface texture: Profile method-Rules and procedures for the assessment of surface texture, Deutsches Institut für Normung
36. Marxer M, Bach C, Keferstein CP (2021) Fertigungsmesstechnik: Alles zu Messunsicherheit, konventioneller Messtechnik und Multisensorik. https://doi.org/10.1007/978-3-658-34168-8.pdf
37. Huang C, Kyvelou P, Zhang R, Britton TB, Gardner L (2022) Mechanical testing and microstructural analysis of wire arc additively manufactured steels. Mater Des 216:110544. https://doi.org/10.1016/j.matdes.2022.110544
38. Elmer JW, Allen SM, Eagar TW (1989) Microstructure development during solidification of stainless-steel alloys. Metall Trans A 20:2117–2131
39. Fu JW, Yang YS (2013) Origin of the lathy ferrite in AISI 304 stainless steel during directional solidification. J Alloys Compd 5802:191–194. https://doi.org/10.1016/J.JALLCOM.2013.05.107
40. Mirshekari GR, Tavakoli E, Atapour M, Sadeghian B (2014) Microstructure and corrosion behaviour of multipass gas tungsten arc welded 304L stainless steel. Mater Des 55:905–911. https://doi.org/10.1016/J.MATDES.2013.10.064
41. de Lima JS, da Silva Neto JF, Maciel TM, Lopez EAT, de Santana RAC, de Abreu Santos TF (2024) Effect of wire arc additive manufacturing parameters on geometric, hardness, and microstructure of 316LSi stainless steel preforms. Int J Adv Manuf Technol 131:5981–5996. https://doi.org/10.1007/s00170-024-13240-4
42. Wang P, Zeng J, Lou D, Zheng W, Zheng S, Chen B, Gao Z (2025) Nonlinear ultrasonic characterization of processing defects in wire arc additive manufacturing 316L stainless steel. Materials 18(4):805. https://doi.org/10.3390/ma18040805
43. Rodrigues TA, Duarte V, Miranda RM, Santos TG, Oliveira JP (2019) Current status and perspectives on wire and arc additive manufacturing (WAAM). Materials 12(7):1121. https://doi.org/10.3390/ma12071121
44. Iqbal H, Ascari A, Fortunato A, Liverani E (2024) Elucidating the effects of metal transfer modes and investigating the material properties in wire-arc additive manufacturing (WAAM). Prog Addit Manuf 10:3335–3360. https://doi.org/10.1007/s40964-024-00808-5
45. Lambiase F, Yanala PB, Paoletti A (2025) Thermal, microstructural, and mechanical characterization of early-stage deposition in wire arc additive manufacturing. Int J Adv Manuf Technol 138:953–970. https://doi.org/10.1007/s00170-025-15561-4
46. Palmeira Belotti L, van Dommelen JAW, Geers MGD, Goulas C, Ya W, Hoefnagels JPM (2022) Microstructural characterisation of thick-walled wire arc additively manufactured stainless steel. J Mater Process Technol 299:117373. https://doi.org/10.1016/j.jmatprotec.2021.117373
47. Sasikumar C, Oyyaravelu R (2024) Mechanical properties and microstructure of SS 316L created by WAAM based on GMAW. Mater Today Commun 38:107807. https://doi.org/10.1016/j.mtcomm.2023.107807
48. ISO-14343 (2017) Welding consumables—wire electrodes, strip electrodes, wires and rods for arc welding of stainless and heat resisting steels-classification
49. Chen X, Li J, Cheng X, He B, Wang H, Huang Z (2017) Microstructural and mechanical properties of the austenitic stainless steel 316L fabricated by gas metal arc additive manufacturing. Mat Sci Eng A 703:567–577. https://doi.org/10.1016/j.msea.2017.05.024
50. Wang L, Xue J, Wang Q (2019) Correlation between arc mode, microstructure, and mechanical properties during wire arc

additive manufacturing of 316L stainless steel. Mat Sci Eng A. https://doi.org/10.1016/j.msea.2019.02.078
51. Wang C, Liu TG, Zhu P, Lu YH, Shoji T (2020) Study on microstructural and tensile properties of 316L stainless steel fabricated by CMT wire and arc additive manufacturing. Mat Sci Eng A. https://doi.org/10.1016/j.msea.2020.140006
52. Kannan AR, Kumar SM, Pramod R, Shanmugam NS, Vishnukumar M, Naveenkumar S (2021) Microstructural characterization and mechanical integrity of stainless steel 316L clad layers deposited via wire arc additive manufacturing for nuclear applications. Mat Sci Eng Technol 52(6):617–623. https://doi.org/10.1002/mawe.202000242
53. Xie B, Xue J, Ren X (2020) Wire arc deposition additive manufacturing and experimental study of 316L stainless steel by CMT + P process. Metals 10(11):1419. https://doi.org/10.3390/met10111419
54. Wu W, Xue J, Wang L, Zhang Z, Hu Y, Dong C (2019) Forming process, microstructure, and mechanical properties of thin walled 316L stainless steel using speed-cold-welding additive manufacturing. Metals 9(1):109. https://doi.org/10.3390/met9010109
55. Ye C et al (2020) Microstructure and mechanical properties of the 316 stainless steel nuclear grade experimental component made by wire and arc additive manufacturing. Proc Inst Mech Eng Part C J Mech Eng Sci. https://doi.org/10.1177/0954406220920692
56. Moore P, Addison A, Nowak-Coventry M (2019) Mechanical properties of wire plus arc additive manufactured steel and stainless steel structures. Weld World 63:1521–1530. https://doi.org/10.1007/s40194-019-00775-4
57. Jin W, Zhamg C, Jin S, Tian Y, Wellmann D, Liu W (2020) Wire arc additive manufacturing of stainless steels: a review. Appl Sci 10(5):1563. https://doi.org/10.3390/app10051563
58. Caballero A, Ding J, Ganguly S, Williams S (2019) Wire + arc additive manufacture of 17–4 PH stainless steel: effect of different processing conditions on microstructure, hardness, and tensile strength. J Mater Process Technol 268:54–62. https://doi.org/10.1016/j.jmatprotec.2019.01.007
59. Jin W, Zhang C, Jin S, Tian Y, Wellmann D, Liu W (2020) Wire arc additive manufacturing of stainless steels: a review. Appl Sci 10(5):1563. https://doi.org/10.3390/app10051563
60. ASTM E384-23 (2023) Standard test method for microindentation hardness of materials. ASTM International, West Conshohocken, PA, USA
61. Jafarzad-Shayan MN et al (2023) Microstructural heterogeneity and exceptional mechanical properties in a wire-arc additively manufactured stainless steel. Mat Sci Eng A 24:145473. https://doi.org/10.1016/j.msea.2023.145473
62. Zhu Z, Ma X, Wang C, Mi G, Zheng S (2020) The metallurgical behaviours and crystallographic characterstic on macro deformation mechanism of 316L laser-MIG hybrid welded joint. Mater Des 194:108893. https://doi.org/10.1016/jmatdes.2020.108893
63. Wanni J, Michopoulos JG, Achuthan A (2022) Influence of cellular subgrain feature on mechanical deformation and properties of directed energy deposited stainless steel 316L. Addit Manuf 51:102603. https://doi.org/10.1016/j.addma.2022.102603
64. Romero-Resendiz L et al (2022) Heterostructured stainless steel: properties, current trends, and future perspectives. Mater Sci Eng R Rep 150:100691. https://doi.org/10.1016/j.mser.2022.100691
65. Callister WD, Rethwisch DG (2018) Materials science and engineering: an introduction, 10th edn. Wiley, New York